A&A 489, 173–194 (2008)
DOI: 10.1051/0004-6361:200809677

Astronomy & Astrophysics

The evolution of planetary nebulae

V. The diffuse X-ray emission⋆

M. Steffen, D. Schönberner, and A. Warmuth

Astrophysikalisches Institut Potsdam, An der Sternwarte 16, 14482 Potsdam, Germany
e-mail: [msteffen;deschoenberner;awarmuth]@aip.de

Received 28 February 2008 / Accepted 13 July 2008

ABSTRACT

Context. Observations with space-borne X-ray telescopes revealed the existence of soft, diffuse X-ray emission from the inner regions of planetary nebulae. Although the existing images support the idea that this emission arises from the hot shocked central-star wind which fills the inner cavity of a planetary nebula, existing models have difficulties to explain the observations consistently.
Aims. We investigate how the inclusion of thermal conduction changes the physical parameters of the hot shocked wind gas and the amount of X-ray emission predicted by time-dependent hydrodynamical models of planetary nebulae with central stars of normal, hydrogen-rich surface composition.
Methods. We upgraded our 1D hydrodynamics code NEBEL by to account for energy transfer due to heat conduction, which is of importance at the interface separating the hot shocked wind gas ("hot bubble") from the much cooler nebular material. With this new version of NEBEL we recomputed a selection of our already existing hydrodynamical sequences and obtained synthetic X-ray spectra for representative models along the evolutionary tracks by means of the freely available CHIANTI package.
Results. Heat conduction leads to lower temperatures and higher densities within a bubble and brings the physical properties of the X-ray emitting domain into close agreement with the values derived from observations. The amount of X-rays emitted during the course of evolution depends on the energy dumped into the bubble by the fast stellar wind, on the efficiency of "evaporating" cool nebular gas via heat conduction, and on the bubble's expansion rate. We find from our models that the X-ray luminosity of a planetary nebula increases during its evolution across the HR diagram until stellar luminosity and wind power decline. Depending on the central-star mass and the evolutionary phase, our models predict X-ray [0.45−2.5 keV] luminosities between 10^{-8} and 10^{-4} of the stellar bolometric luminosities, in good agreement with the observations. Less than 1% of the wind power is radiated away in this X-ray band. Although temperature, density, and also the mass of the hot bubble is significantly altered by heat conduction, the dynamics of the whole system remains practically the same.
Conclusions. Heat conduction allows the construction of nebular models which predict the correct amount of X-ray emission and at the same time are fully consistent with the observed mass-loss rate *and* wind speed. Thermal conduction must be considered as a viable physical process for explaining the diffuse X-ray emission from planetary nebulae with closed inner cavities. Magnetic fields must then be absent or extremely weak.

Key words. conduction – hydrodynamics – planetary nebulae: general – radiative transfer – X-rays: stars

1. Introduction

The modern, very successful concept for the formation and evolution of the main structures of Planetary Nebulae (PNe) is based on the dynamical effects caused by (i) the interaction of a rapidly varying central-star stellar wind with the slow AGB wind ejected earlier; and (ii) the heating of this circumstellar material by photoionization. The wind from the central star is very fast, exceeding in most cases 1000 km s^{-1}, and passes through a shock before making contact with the dense slow AGB wind. A tenuous but very hot ($\gtrsim 10^7$ K) "bubble" is formed since 9/16 of the kinetic wind energy is converted into internal energy behind a strong adiabatic shock. The bubble is separated from the outer, much cooler nebular gas by a contact discontinuity (or contact surface). The bubble's thermal expansion accelerates the inner layers of the PN. For recent reviews see Schönberner & Steffen (2003) and Steffen & Schönberner (2006).

The shocked wind gas including the thin transition regime towards the PN proper are the likely sites of diffuse X-ray emission, mainly by thermal bremsstrahlung and line emission (Volk & Kwok 1985). Any positive detection of diffuse X-ray emission coming from the inner cavities enclosed by nebular shells is a direct confirmation of the wind interaction scenario as sketched above. Thus there was considerable interest to observe selected PNe with X-ray satellites once they became available. Since the surface brightness in X-rays is expected to be quite small (see Volk & Kwok 1985), only very few positive detections have been reported to date. Summaries of X-ray observations of PNe conducted to date with the different satellites are presented in Chu et al. (2003), Guerrero (2006), and Kastner (2007).

Although the observational confirmation of the existence of shocked wind material was very gratifying, the properties of the X-ray emitting gas were disturbing. It turned out that the X-ray spectra are rather soft, indicating temperatures of

⋆ Dedicated to the memory of M. Perinotto, a dear friend and esteemed colleague who died unexpectedly and much too early on August 15, 2007.

only $\approx(1\ldots3)\times10^6$ K. The electron densities of the emitting volumes vary between about 20 and 200 cm^{-3}. These results are in sharp contrast with theoretical expectations since the *observed* wind velocities and mass-loss rates demand bubble temperatures of $\approx10^7\ldots10^8$ K, and electron densities far *below* the observed ones.

Akashi et al. (2006) and Akashi et al. (2007) proposed that the remains of the much slower wind blown during the early PN evolution ("early wind") when heat conduction is unimportant are responsible for the properties of the observed X-ray emission. Also collimated outflows (jets) can play a role. So it appears that several physical mechanisms exist (heat conduction and/or mixing, early wind, jets) which all may contribute to the X-ray emission, as pointed out by Soker & Kastner (2003). The jet-wind interaction has recently been studied in detail by Akashi et al. (2008).

In two fundamental papers on the properties of interstellar bubbles by Castor et al. (1975) and Weaver et al. (1977) it was demonstrated that heat conduction by electrons across the contact surface which separates the hot shocked wind gas from the much cooler swept-up matter is a natural mechanism to account for the observed X-ray and EUV line emissions. Heat conduction enforces "evaporation" of cool gas into the hot bubble, leading to a shell of matter at the bubble's outer edge with properties just ideal for explaining the observed X-ray and EUV line emission.

Since planetary nebulae are virtually scaled down versions of the interstellar bubbles (or H II regions), heat conduction should be important for them as well. To our knowledge, Soker (1994) was the first to look into the consequences of heat conduction in PNe. He concluded that the observed X-ray emission must come from the heat conduction front, and not from the hot bubble as a whole. Heat conduction is also capable of explaining the unusually strong UV lines (e.g. of O VI) seen in some PNe, which cannot be produced by regular photoionization. Soker (1994) noted also that weak tangential magnetic fields would suppress heat conduction very effectively, and hence also the X-ray emission. But even without magnetic fields X-rays from old, large PNe may escape detection because the X-ray surface brightness falls below the detection limit of existing X-ray satellites. We note in passing that the same considerations apply to wind-blown bubbles around massive stars as well (cf. Wrigge et al. 1994).

Despite of their potential importance, quantitative theoretical calculations of X-ray and EUV emissions from PNe based on the concept of heat conduction are rare. Zhekov & Perinotto (1996, 1998) succeeded in developing analytical solutions based on the concept of Weaver et al. (1977) and were able to present quantitative predictions for a few specified cases. Using analytical solutions of heat conduction, Gruendl et al. (2004) modelled the transition layers between the hot bubble and the nebular regime for NGC 6543 in order to compute the O VI emission lines seen in the FUSE spectra.

Two hydrodynamical studies addressed recently the issue of X-ray emission from planetary nebulae (Stute & Sahai 2006; Akashi et al. 2007). The basic philosophy of both studies is to avoid thermal conduction and to select the properties of the wind such that temperature and density of the X-ray emitting gas agree with the observations. No relation between stellar parameters and wind properties is considered, and the feedback of radiation to the hydrodynamics is neglected. To explain the observed X-ray luminosities, these authors came up with wind parameters which disagree strongly with both the predictions of the theory of radiation-driven winds (e.g. Pauldrach et al. 1988) *and* with the directly observed mass-loss rates and wind speeds of the objects in question. More precisely, the necessary mass-loss rates are too large and the corresponding wind speeds too low – by as much as a factor 5[1].

The results of Akashi et al. (2007) are particularly interesting. Consistence with existing observations in terms of X-ray luminosity and temperature of the X-ray emitting gas could be achieved only for rapidly decaying central-star winds: while the wind speed increases linearly with time, the mass-loss rate must decline quite rapidly to very small values (see Akashi et al. 2007, Figs. 6 and 8 therein). For the best choice of Akashi et al. (2007), the central-star wind reaches 10^{-10} $M_\odot$ yr^{-1} already at a modest wind speed of only 750 km s^{-1}.

We iterate that combinations of mass-loss rates and outflow speeds as they are found in Akashi et al. (2007) are in severe conflict with both current theories of radiation-driven winds from hot stars (see Fig. 2 in Sect. 3, for details) *and* with the observations (see Table 3 in Sect. 5.2), with the apparent exception of NGC 2392. In our opinion the existing studies of the X-ray emission from planetary nebulae which neglect thermal conduction by electrons are therefore far from being convincing. After all, thermal conduction is a physical process inherent to all hydrodynamical systems and becomes important in rarefied plasmas wherever the mean free path of the electrons is large enough. Thermal conduction can *only* be modified or even suppressed by the existence of magnetic fields (cf. Borkowski et al. 1990).

Since no self-consistent radiation-hydrodynamics computations including heat conduction have been performed to date[2], and urged by the fact that the new observations which became available by the Chandra and XMM-Newton satellites lack a convincing interpretation by detailed modeling, we decided to update our 1D radiation-hydrodynamics code NEBEL by incorporating a thermal conduction module. We recomputed then some of our sequences from Perinotto et al. (2004, Paper I hereinafter) with heat conduction self-consistently included. Based on the new thermal structure of the bubble we modelled the X-ray and EUV emissions at selected positions along the evolutionary sequences by using the well-documented CHIANTI code.

We emphasize that in our study (i) wind and stellar evolution are consistently connected within the framework of the theory of radiation-driven winds; and (ii) no fit to the data by manipulating the models is done. It is our belief that only with such an approach it is possible to interprete the data appropriately and to deduce meaningful constraints regarding the relevant physics. Obviously, our approach is only applicable to objects which do not depart too much from sphericity, have closed shells where a bubble of shocked, hot wind gas is able to exist, and have central stars of normal, hydrogen-rich surface composition.

We avoid to discuss in the present work objects with [WC] central stars for two reasons: (i) their evolution is at present not known; and (ii) the physics of heat conduction in hydrogen-free and carbon-rich plasmas has still to be worked out. We note that the X-ray emission from a hydrogen-free plasma is expected to be stronger, making it more likely to detect extended X-ray emission from PNe with [WC] central stars. The present number of positive detections is, however, too small as to make any definitive statements concerning the ratio of PNe X-ray sources with normal and [WC] central stars, respectively.

[1] The only exception is the central star of NGC 2392 whose wind speed is much too low for its position in the Hertzsprung-Russell diagram.

[2] Mellema & Frank (1995) computed the X-ray emission of their 2D hydrodynamics models, but heat conduction was not considered.

Table 1. Elemental abundances, ϵ_i, used in the computations of our hydrodynamical models, in (logarithmic) number fractions relative to hydrogen, $\log \epsilon_i = \log(n_i/n_H) + 12$.

H	He	C	N	O	Ne	S	Cl	Ar
12.00	11.04	8.89	8.39	8.65	8.01	7.04	5.32	6.46

The computational details of how the thermal conduction is treated are described in the Sect. 2, followed by a discussion of the resulting bubble structures in Sect. 3. Section 4 is devoted to the X-ray emission emerging from the conduction front and how it develops with time. In Sect. 5 we discuss extensively how our models compare with the existing observations. The paper concludes with Sect. 6. Part of the results presented here can be found in Schönberner et al. (2006).

2. The computations

2.1. The hydrodynamical models

The basic idea behind our modeling is to couple a spherical circumstellar envelope, being the relic of the strong wind on the asymptotic giant branch (AGB), to a post-AGB star model of certain mass and to follow numerically the hydrodynamical evolution of the envelope across the Hertzsprung-Russell diagram towards the white-dwarf cooling path. This is achieved by applying our 1D radiation-hydrodynamics code NEBEL as described in more detail in Perinotto et al. (1998). The inner boundary condition in terms of density and velocity is provided by the variable central star wind. For the ionizing photon flux the star is assumed to radiate as a black body for each given effective temperature.

The radiation part of our hydrodynamics code, CORONA, is described in Marten & Sczcerba (1997). We point out that this code is designed to compute ionization, recombination, radiative heating and line cooling fully time-dependently. At each volume element, the cooling function is composed of the contributions of all the ions considered and computed according to the actual plasma parameters. For each chemical element listed in Table 1, up to 12 ionization stages are taken into account, amounting to a total of 76 ions.

In Paper I a very detailed description of how the nebular properties depend on the chosen initial envelope configurations and central-star models is given. For the present study we selected representative sequences and recomputed them with and without heat conduction included. The new simulations consider 9 chemical elements instead of 6, with abundances as listed in Table 1. A compilation of the sequences investigated here is given in Table 2. The 0.595 $M_\odot$ post-AGB model has been introduced in Schönberner et al. (2005b). Sequence No. 10a is a variant of sequence No. 10 of Paper I with the AGB mass-loss rate doubled. Note that the luminosities listed in Table 2 correspond to the early part of the post-AGB evolution. They decrease slowly during the evolution across the Hertzsprung-Russell diagram.

2.2. The treatment of electron heat conduction

2.2.1. Physical description

Electron heat conduction is described as a diffusion process, with the heat flux $\boldsymbol{q}$ given by

$$\boldsymbol{q} = -D\,\nabla T_e. \tag{1}$$

Table 2. Hydrodynamical sequences of model planetary nebulae used in this work. The sequence numbers correspond to Table 1 in Paper I and Table 2 in Schönberner et al. (2005b), but the additional notation "HC" and "HC2" indicates that heat conduction is included according to method 1 and 2, respectively (see Sect. 2.2). The stellar luminosities refer to $T_{\rm eff}$ = 30 000 K, and the peak mass-loss rate of the AGB hydrodynamical simulation (6, 6a) is about $1 \times 10^{-4}\ M_\odot\ {\rm yr}^{-1}$. TYPE indicates the structure adopted for the AGB envelope: "A" means constant mass loss rate, $\rho \simeq r^{-2}$, "B" means structure from hydrodynamical simulation (see Paper I for details).

No.	M ($M_\odot$)	L ($L_\odot$)	$\dot{M}_{\rm agb}$ ($M_\odot\ {\rm yr}^{-1}$)	$v_{\rm agb}$ (km s^{-1})	TYPE
22	0.565	3981	3×10^{-5}	10	A
22-HC2	0.565	3981	3×10^{-5}	10	A
6a	0.595	5593	Hydro. sim.	≃12	C
6a-HC	0.595	5593	Hydro. sim.	≃12	C
6a-HC2	0.595	5593	Hydro. sim.	≃12	C
6	0.605	6280	Hydro. sim.	≃12	C
6-HC	0.605	6280	Hydro. sim.	≃12	C
6-HC2	0.605	6280	Hydro. sim.	≃12	C
10	0.696	11 615	1×10^{-4}	15	A
10-HC2	0.696	11 615	1×10^{-4}	15	A
10a-HC	0.696	11 615	2×10^{-4}	15	A
10a-HC2	0.696	11 615	2×10^{-4}	15	A

Following Spitzer (1962) and Cowie & McKee (1977), the electron mean free path λ is a function of electron temperature, T_e, and electron number density, n_e, and can be written as

$$\lambda = 2.625 \times 10^5\ T_e^2/n_e/\ln\Lambda \quad [{\rm cm}], \tag{2}$$

where the Coulomb Logarithm, $\ln\Lambda$, can be approximated as

$$\ln\Lambda = \begin{cases} 9.425 + 3/2\ \ln T_e - 1/2\ \ln n_e, & T_e \le 4.2 \times 10^5\ {\rm K}, \\ 22.37 + \quad\ \ln T_e - 1/2\ \ln n_e, & T_e > 4.2 \times 10^5\ {\rm K}, \end{cases} \tag{3}$$

for a pure hydrogen plasma. The diffusion coefficient D is then given by

$$D = 7.04 \times 10^{-11}\ \lambda\ n_e\ T_e^{1/2} \quad [{\rm erg\,s^{-1}\,K^{-1}\,cm^{-1}}]. \tag{4}$$

At high T_e and low n_e, the electron mean free path λ becomes very large according to Eq. (2) (actually it can become much larger than the dimensions of the "hot bubble"), and the diffusion approximation is no longer valid. Rather, the heat flux cannot exceed the saturation limit

$$\boldsymbol{q}_{\rm sat} = 1.72 \times 10^{-11}\ T_e^{3/2} n_e \quad [{\rm erg\,cm^{-2}\,s^{-1}}]. \tag{5}$$

This is an approximate upper limit expressing the fact that the heat flux cannot be larger than the heat content, $3/2\,n_e k T_e$, times a characteristic electron transport velocity, $v_{\rm char}$. For a more detailed derivation of Eq. (5) see Cowie & McKee (1977).

2.2.2. Numerical treatment

Each time step Δt of the hydrodynamical simulations is divided into 3 successive steps for updating the state vector $\boldsymbol{Q}$ (operator splitting):

(a) $\boldsymbol{Q}(t) \Rightarrow$ advection $\Rightarrow \boldsymbol{Q_1}(t + \Delta t)$;
(b) $\boldsymbol{Q_1}(t + \Delta t) \Rightarrow$ heat conduction $\Rightarrow \boldsymbol{Q_2}(t + \Delta t)$
(1st energy update at constant mass density ρ);
(c) $\boldsymbol{Q_2}(t + \Delta t) \Rightarrow$ radiation $\Rightarrow \boldsymbol{Q}\ (t + \Delta t)$
(2nd energy update at constant mass density ρ).

Ionization is frozen during step (b), being updated subsequently in step (c). For step (b), we solve the diffusion equation in spherical coordinates,

$$\frac{\partial E}{\partial t} = \rho c_\mathrm{v} \frac{\partial T_\mathrm{e}}{\partial t} = \frac{1}{r^2} \frac{\partial}{\partial r} \left(r^2 \, D \, \frac{\partial T_\mathrm{e}}{\partial r} \right), \tag{6}$$

(E: internal energy per unit volume, c_v: specific heat at constant volume, r: radial coordinate) with a fully implicit, standard numerical method. No additional constraints are imposed on the time step by this implicit energy update.

The diffusion coefficient D is evaluated at the *cell boundaries* from the local physical conditions according to Eq. (4), with λ replaced by $\overline{\lambda}$ (see below) to take into account the effect of saturation. In order to take care of the fact that the diffusion coefficient itself depends on temperature, we have adopted the following procedure to obtain the temperature update from initial temperature T_1 to final temperature T_2 due to electron heat conduction acting over the time interval Δt : (i) we calculate the initial diffusion coefficient $D_0 = D(T_1)$; (ii) starting from T_1, we solve the diffusion equation Eq. (6) for time step $\Delta t/2$ with $D = D_0$ taken to be constant over time, resulting in intermediate temperature $T_{1/2}$; (iii) we calculate the intermediate diffusion coefficient $D_{1/2} = D(T_{1/2})$; (iv) starting again from T_1, we solve the diffusion equation for the full time step Δt with $D = D_{1/2}$ taken to be constant over time, resulting in the final temperature state T_2. This procedure turned out to be perfectly adequate: comparison with a test calculation using 10 intermediate time steps instead of 1 gave practically identical results.

In the framework of the diffusion approximation, Eq. (1), saturation effects can be crudely accounted for by limiting the mean free path λ. However, there is some arbitrariness involved in this approach, and it is not clear which recipe gives the most realistic results. We have tried two extreme methods:

- In method 1, we limit the electron mean free path to a fraction of the spatial resolution of the numerical grid, i.e. we calculate $\overline{\lambda}$ as

$$\overline{\lambda}_1 = \min\{f \times \Delta r, \quad 2.625 \times 10^5 \, T_\mathrm{e}^2 / n_\mathrm{e} / \ln \Lambda\}, \tag{7}$$

  where Δr is the local spacing of the radial grid. Choosing the constant $f = 0.244$ ensures that the conductive heat flux can never exceed the saturation heat flux given by Eq. (5): in regions where the limiter is active, i.e. where $\overline{\lambda}_1 = 0.244 \cdot \Delta r$, we obtain $\boldsymbol{q} = \boldsymbol{q}_\mathrm{sat} \cdot \Delta r \, \boldsymbol{\nabla} T_\mathrm{e} \, / T_\mathrm{e} \approx \boldsymbol{q}_\mathrm{sat} \cdot \Delta T_\mathrm{e} / T_\mathrm{e}$, where ΔT_e is the temperature difference between two adjacent grid points. Hence, the limiting flux can only be reached at the sharp edge of a hot region where $|\Delta T_\mathrm{e}| \approx T_\mathrm{e}$. A drawback of this method is that $\overline{\lambda}_1$, and hence the results, depend explicitly on the numerical resolution Δr. Sequences computed with this approach are denoted in Table 2 with label "HC".
- In method 2, we limit the electron mean free path according to the interpolation formula

$$\frac{1}{\overline{\lambda}_2} = \frac{1}{2.625 \times 10^5 \, T_\mathrm{e}^2 / n_\mathrm{e} / \ln \Lambda} + 4.105 \, \frac{|\boldsymbol{\nabla} T_\mathrm{e}|}{T_\mathrm{e}} \, . \tag{8}$$

  As with the first method, the conductive heat flux cannot exceed the saturation heat flux given by Eq. (5): in regions where $\lambda \ll \Delta r$, the first term on the right hand side of Eq. (8) dominates, and $\overline{\lambda}_2 = \lambda$, i.e. the limiter is inactive. When $\lambda \gg \Delta r$, the second term on the right hand side of Eq. (8) dominates, so $\overline{\lambda}_2 = 0.244 \cdot T_\mathrm{e} / |\boldsymbol{\nabla} T_\mathrm{e}|$, and $\boldsymbol{q} = \boldsymbol{q}_\mathrm{sat}$. Sequences with this treatment of thermal conduction are indicated by the label "HC2" (see Table 2).

The two methods represent the extreme cases. Method 2 essentially gives the saturation flux Eq. (5) wherever the unlimited flux would exceed this value, while method 1 generally yields much smaller fluxes, reaching the saturation flux only under extreme conditions.

As a final remark we note that we have not attempted to correct the calculation of the diffusion coefficient for the fact that the actual chemical composition of the nebular matter is not pure hydrogen.

2.3. The CHIANTI code and the computation of the X-ray emission

For obtaining the X-ray emission of our model PNe it is necessary to compute a synthetic optically thin X-ray spectrum for each radial shell of the model, since the different values for T_e, n_e and n_p at each shell result in unique spectral characteristics. The spectra were calculated using the CHIANTI software package (Dere et al. 1997), which has been used extensively by the astrophysical and solar communities. CHIANTI consists of an up-to-date set of atomic data for a large number of ions of astrophysical interest, and also includes a number of ancillary data and a suite of useful routines.

Our synthetic spectra were computed with version 5.1 of CHIANTI (Landi & Phillips 2005), which includes the most recent atomic data. Only radial shells with $T_\mathrm{e} > 10^5$ K were considered, since the contribution of cooler layers is negligible in the X-ray range. With the input of T_e, n_e and n_p for a given volume element, individual spectra are then synthesized, including the contribution due to lines and various continua (free-free, free-bound and two-photon continuum). We have used the ion fractions from Mazzotta et al. (1998), under the assumption of ionization equilibrium. The elemental abundances used are either those listed in Table 1 or solar values for the elements not considered in our hydrodynamics simulations.

Each individual spectrum actually represents the emission (in erg s^{-1} cm^{-3} Å^{-1}) from a unit volume. In order to determine the total X-ray emission, the averaged spectrum, and the brightness distribution in the plane of the sky, we must perform appropriate integrations over our spectra, taking the (spherical) geometry of the model into account. The multiplication of an individual spectrum with the volume of the corresponding radial shell gives the total emission from that shell, and the summation over all shells emitting in X-rays then yields the total spectrum. An integration over a certain wavelength range then results in a well-defined total X-ray luminosity, L_X (in erg s^{-1}).

For determining the brightness distribution in the plane of sky (in erg cm^{-2} s^{-1} sr^{-1}), the integration is performed along the line of sight (perpendicular to the plane of sky) for a series of impact parameters (up to about 400).

The computation of the complete X-ray spectrum and luminosity is rather time consuming and thus only performed for selected models along an evolutionary sequence. Such a post-facto computation of the X-ray emission is somewhat inconsistent with the hydrodynamics since at least part of the energy lost from the bubble by X-rays, viz. the energy loss due to ions not considered in our simulations (cf. Table 1 and Sect. 2.1), is not included in its energy budget. However, since the X-ray luminosity computed by means of the CHIANTI code is only a very small fraction of the total radiation losses from the hot bubble as already provided by the NEBEL code (see Sect. 3.3, Fig. 7), a somewhat incomplete consideration of the X-ray loss in the

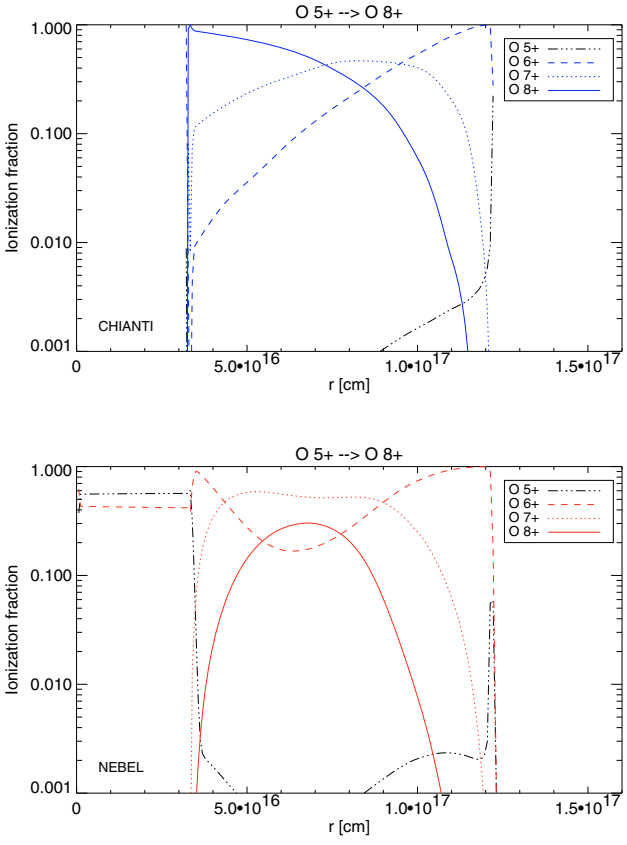

Fig. 1. The fractions of the last 4 ionization stages of oxygen within a typical PN bubble selected from sequence No. 6a-HC2. The model parameters are $L = 5205\ L_\odot$ and $T_{\rm eff} = 71\,667$ K at $t = 5642$ yr. Heat conduction is considered according to method 2. The central star is at the origin, the (reverse) wind shock at $r = 3.2 \times 10^{16}$ cm, and the conduction front at 1.22×10^{17} cm. *Top*: predictions from CHIANTI. Note that the CHIANTI code is only applicable to the region embraced by the wind shock and the conduction front. *Bottom*: predictions from our time-dependent computations with NEBEL. Beyond the conduction front, i.e. in the "cool" nebular gas, the fractions of the displayed ions drop rapidly to virtually zero.

bubble's energy budget has absolutely no consequences for the dynamics of the whole system.

We checked also whether the ionization structures predicted by our hydrodynamics code and by CHIANTI are consistent with each other. Figure 1 gives an example for the ionization structure of oxygen within a typical bubble and compares the predictions of the CHIANTI code (top panel) with our time-dependent NEBEL/CORONA code (bottom panel). Note that the ionization fractions computed by CHIANTI are *equilibrium values* and a function of the electron temperature only. In contrast, the ion densities computed by NEBEL/CORONA are the result of solving explicitly the time-dependent rate equations for the local temperatures and densities, and accounting for advection. Hence, the NEBEL results are expected to approach the equilibrium solution provided by the CHIANTI code only for sufficiently high electron density and low flow velocity.

The bottom panel of Fig. 1 illustrates nicely how the ionization of oxygen changes while the gas passes through the wind shock: the main ionization stages of oxygen in the freely streaming wind are those of O^{5+} and O^{6+}. After passing through the wind shock, the ionization switches to O^{6+}, O^{7+} and O^{8+} because of the very large post-shock temperatures. Also close to the conduction front where heated matter streams inwards (relative to the front, see Borkowski et al. 1990, Fig. 4), we see a small influence of advection (compare the distribution of O^{5+} around $r = 1.2 \times 10^{17}$ cm in both panels of Fig. 1).

The dense regions above 10^6 K close to the conduction front, i.e. for $r \gtrsim 10^{17}$ cm in Fig. 1, contribute most to the bubble's X-ray emission, as we will see later. There we have reasonable agreement between the CHIANTI and NEBEL predictions. The remaining differences are likely due to differences in the atomic data used. Considering the other uncertainties involved in this investigation, like, e.g., the wind model, the assumption of sphericity, and, last but not least, the observational data, we think that our approach of computing the X-ray emission post-facto from the nebular models by using the CHIANTI code is well justified.

3. Heat conduction and bubble structure

In this section we discuss in detail the results following from our numerical concept introduced in Sect. 2.2 and compare them with our previous simulations without heat conduction. For this purpose we used the sequences Nos. 6a, 6a-HC and 6a-HC2, all of which are based on the 0.595 $M_\odot$ post-AGB model with the same initial envelope (cf. Table 2) but with a different treatment of heat conduction.

3.1. The wind model

Figure 2 illustrates the evolutionary properties of the central star and its wind in terms of post-AGB time and stellar effective temperature. The relevant quantity for powering any X-ray emission is the mechanical luminosity of the stellar wind, $L_{\rm wind} = \dot{M}_{\rm wind}\, v_{\rm wind}^2/2$. It is important to emphasize that, according to the theory of radiation-driven winds for standard hydrogen-rich chemical composition in the formulation of Pauldrach et al. (1988), *the mass-loss rate and the wind speed depend on the stellar parameters (mass, luminosity, effective temperature).* Based on these wind prescriptions, the mechanical energy transported by the wind increases during the evolution across the Hertzsprung-Russell diagram, simply because the slowly decreasing mass-loss rate is over-compensated by the increasing wind speed (Fig. 2, upper right). However, when the hydrogen shell becomes exhausted, the mass loss rate drops sharply in line with the stellar bolometric luminosity, causing also the mechanical wind power to drop considerably since the wind speed remains now virtually constant at its maximum value of about 10 000 km s^{-1}.

In any case, the mechanical power remains always rather small and, in this particular case, does not exceed 1% of the stellar photon luminosity (Fig. 2, lower left). According to the wind model used in this work, the maximum of the mechanical power occurs close to maximum stellar temperature. Only very little mass is carried away by the wind during the whole transition to the white-dwarf domain, viz. $\approx 3 \times 10^{-4}\ M_\odot$ (lower right panel), which may be compared with the typical PN mass of a tenth of a solar mass.

We emphasize that *most* of this mass is already lost with low speed during the first 1000 yr of transition to the PN stage! Only during this phase we have wind speeds as low as a few 100 km s^{-1}, i.e. low enough to provide post-shock temperatures of the order of 10^6 K. These mass-loss parameters are typical for those of the "early wind" and are here based on the Reimers (1975) prescriptions (see caption of Fig. 2). The "early-wind" phase is included consistently in our simulations with the appropriate treatment of radiative cooling. The stellar mass lost during

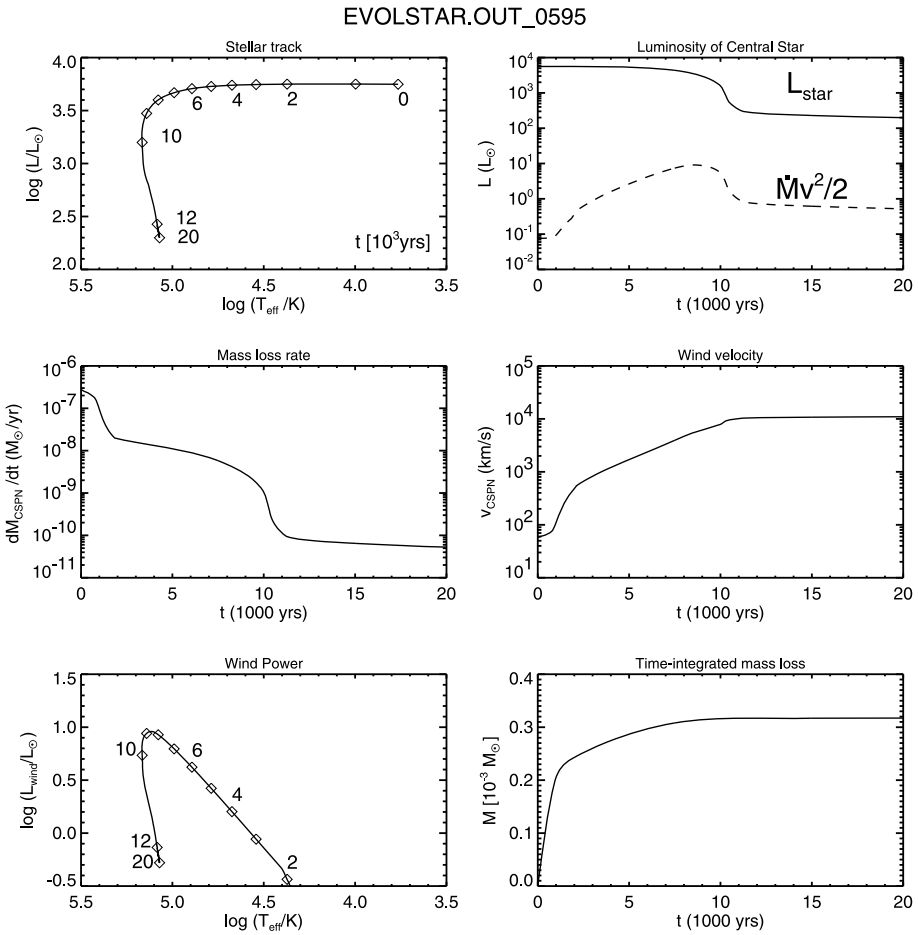

Fig. 2. *Top*: evolutionary path of the 0.595 $M_\odot$ model in the Hertzsprung-Russell diagram with the post-AGB ages, t, indicated along the track (*left*), and the stellar bolometric (solid) and wind (dashed) luminosities vs. age (*right*). *Middle*: mass-loss rate (*left*) and (terminal) wind velocity (*right*). We followed the recommendations of Pauldrach et al. (1988) for the central-star wind ($T_{\rm eff} \geq 25\,000$ K), while we assumed a Reimers wind (Reimers 1975) during the transition to the PN domain (cf. also Paper I). *Bottom*: stellar wind luminosity (power) vs. stellar effective temperature (*left*), again with the post-AGB ages indicated, and the total mass lost by the wind during the post-AGB evolution (*right*).

the following PN stage is only about 8×10^{-5} $M_\odot$, but this material has a very high kinetic energy because of its large speed exceeding 1000 km s^{-1}, leading to post-shock temperatures in excess of 10^7 K.

We close this section on our wind model with a discussion about its relevance for real objects. For this purpose we compared the observed wind luminosities of PNe with diffuse X-ray emission used in Sect. 5 and listed in Table 3 with the predictions of our post-AGB models (see Fig. 3). There is only one apparent discrepancy between theory and observation: the wind power of NGC 2392 is about a factor of 5 below our predictions, a consequence of the exceptionally low wind speed measured for this particular object. The remaining objects from Table 3 (NGC 3242, NGC 6543, NGC 7009) have wind luminosities which are, on the average, only a factor 2 below the theoretical predictions.

Given the large uncertainties of the mass-loss rate determinations, we do not consider a factor of two difference between observed and computed wind powers to be alarming. Moreover, the distances of NGC 3242, NGC 6543, and NGC 7009 used here provide stellar luminosities that are somewhat *below* those for a typical central star of 0.6 $M_\odot$ which is about 5000 $L_\odot$ (cf. Table 3). A corresponding increase of the distances would bring theory and observation in much closer agreement ($L_{\rm wind} \propto$ distance$^{1.5}$).

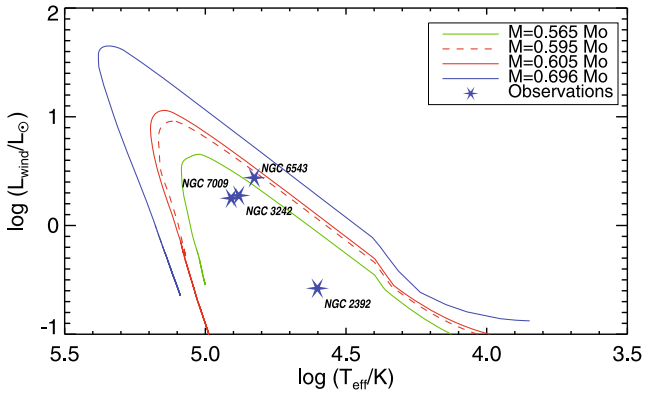

Fig. 3. Stellar wind luminosities vs. effective temperatures for the four mass sequences considered in this work. The observed wind luminosities of PNe with diffuse X-ray emission, taken from the compilation in Table 3, are shown as "star" symbols.

3.2. The influence of thermal conduction

The influence of thermal conduction is illustrated in Fig. 4 where the density and temperature structures of three models at about the same position along the evolutionary path shown in Fig. 2 are compared. As expected, thermal conduction across the bubble/PN interface has a profound impact on the density and thermal structure of the bubble. As a reference, the top panel of Fig. 4 shows the typical temperature / density structure of the shocked wind if thermal conduction is ignored. The gas is very hot ($T_{\rm e} \simeq 8 \times 10^7$ K) and tenuous ($n_{\rm e} \approx 0.5$ cm^{-3}), and these properties do not change much with radius. Such a bubble structure is in sharp contrast to the cases where heat conduction is explicitly considered, as is evident from the middle and bottom panels of Fig. 4.

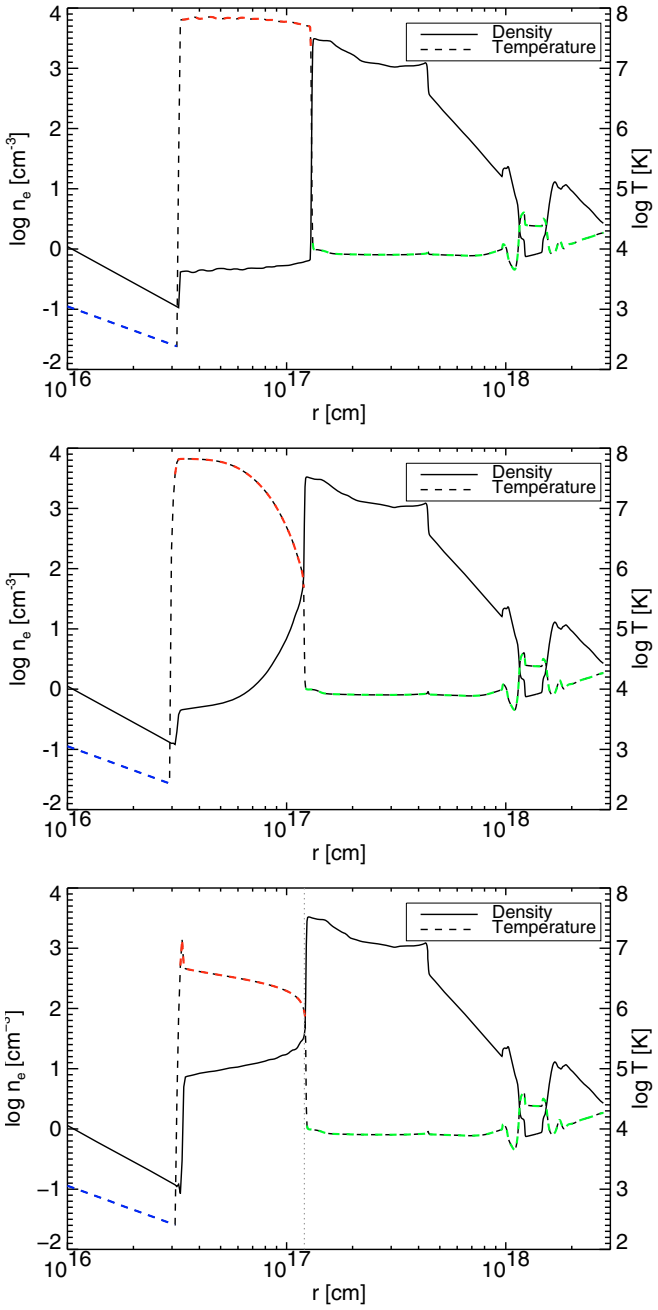

Fig. 4. Radial profiles of electron density (solid, left ordinate) and temperature (dashed, right ordinate) of three models taken from sequences No. 6a (*top*), No. 6a-HC (*middle*) and No. 6a-HC2 (*bottom*), respectively, at about the same positions along the stellar path shown in Fig. 2. The approximate stellar parameters are $L \simeq 5200\ L_\odot$, $T_{\rm eff} \simeq 71\,600$ K at $t \simeq 5640$ yr. The central star is at the origin, and the (reverse) wind shock at $r \simeq 3 \times 10^{16}$ cm. The shocked wind gas, i.e. the bubble, is (in all three cases) between the wind shock and the contact surface/conduction front ($r \simeq 1.3 \times 10^{17}$ cm). The PN proper is bounded by the contact surface/conduction front and an outer shock at $r \simeq 4.4 \times 10^{17}$ cm. The PN is surrounded by the ionized AGB wind whose radial density profile reflects the mass-loss history of the late AGB evolution (Schönberner et al. 1997; Steffen et al. 1998).

Already the treatment of heat conduction according to method 1 leads to a completely different bubble structure: a significant temperature gradient is established, whereby the region close to the conduction front reaches temperatures as low as 10^6 K (Fig. 4, middle panel). The bubble remains virtually isobaric (because of the high sound speed), and an increased matter density must compensate the temperature decrease. This additional mass is provided by a (subsonic) flow of nebular gas heated ("evaporated") at the conduction front (cf. Weaver et al. 1977). Note that the physical conditions immediately behind the (reversed) wind shock are virtually not influenced by heat conduction, i.e. the shock remains fully adiabatic.

Method 2 provides more efficient heat conduction, and hence the thermal structure of the bubble is more homogeneous with smaller temperature and density contrasts between wind shock and conduction front (Fig. 4, bottom panel). The bubble gas is not hotter than about 5×10^6 K (except in a thin region immediately behind the wind shock), and the minimum (electron) density is about 10 cm^{-3}. Because thermal conduction carries energy away from the wind shock, the latter is now not adiabatic anymore: the density jump across the shock is nearly two orders-of-magnitude, in sharp contrast to the heat conduction treatment based on method 1 and the case without heat conduction in which the densities increase only by a factor of four (see Fig. 4, top and middle panel). We note also that the bubble structures seen in Fig. 3 are typical ones which do not change much along the main evolution across the HR diagram. The concept of an ideal contact discontinuity with no mass transfer from one side to the other does not hold anymore: the outer edge of the bubble (=inner edge of the nebula) is now defined by the heat conduction front.

Figure 4 indicates also that *the dynamics of the whole system remains practically unaffected by the physical treatment of the bubble gas*: in all three cases considered, the bubble sizes and the nebular structures are virtually identical (see also Fig. 10).

Heat conduction does not change the total energy budget of the bubble but only transfers thermal energy across the bubble from the wind shock towards the contact surface/conduction front, where it is used to heat and "evaporate" nebular gas. The latter flows inwards relative to the conduction front and remains thereby inside the bubble (see e.g. Weaver et al. 1977). Line cooling can change the bubble's energy content substantially (see Sect. 3.3). However, radiative cooling is confined to a thin surface layer of the hot bubble ($10^4 \ldots 10^5$ K) whose temperature and density structure is not much affected by thermal conduction. Radiative losses are therefore only slightly enhanced in models with heat conduction (cf. Fig. 7). Although the amount of mass "evaporated" from the cold nebular gas exceeds by far the mass injected into the bubble by the stellar wind, it can be totally neglected for the mass budget of the PN proper (see Sect. 3.3).

Figure 5 illustrates the typical bubble structures for two models with different central stars and hence different wind powers and time scales of evolution. The model with the massive central star (0.696 $M_\odot$) has a very compact and dense bubble due to its fast evolution and powerful stellar wind. The other extreme occurs for the model with the least massive central star, (0.565 $M_\odot$), which evolves most slowly and has only a rather modest stellar wind: the bubble is extended and relatively tenuous. Also the mean bubble temperatures reflect the different wind properties: the 0.696 $M_\odot$ model has the largest bubble temperatures of our sequences because the mechanical energy input by the the stellar wind is largest and the bubble size is smallest, as explained in more detail in Sect. 3.3. The case of 0.595 $M_\odot$ shown in the bottom panel of Fig. 4 is intermediate.

3.3. The evolution of the bubble masses

The evolution of the bubble's mass with time is shown in Fig. 6 for the two heat conduction cases considered here. One sees that

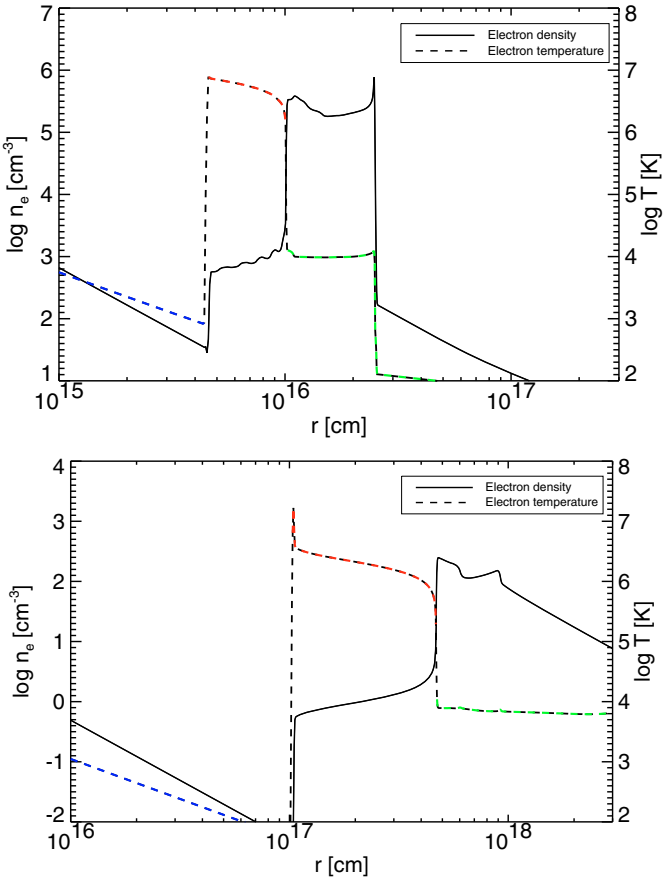

Fig. 5. Radial profiles of electron density (solid, *left ordinate*) and temperature (dashed, *right ordinate*) of two models with different central-star masses. *Top*: 0.696 $M_\odot$ (sequence No. 10-HC2) at t = 301 yr and with L = 11 392 $L_\odot$, $T_{\rm eff}$ = 70 405 K. The large drop of electron density and temperature at $r \simeq 2.5{\times}10^{16}$ cm indicates the position of the ionization front. The reverse wind shock is at $r = 4.5{\times}10^{15}$ cm, the conduction front at $r = 1 \times 10^{16}$ cm. *Bottom*: 0.565 $M_\odot$ (sequence No. 22-HC2) at t = 12 107 yr with L = 3455 $L_\odot$, $T_{\rm eff}$ = 69 906 K. The wind shock is at $1{\times}10^{17}$ cm, the conduction front at $r = 4.5{\times}10^{17}$ cm. Note the different ranges the electron density.

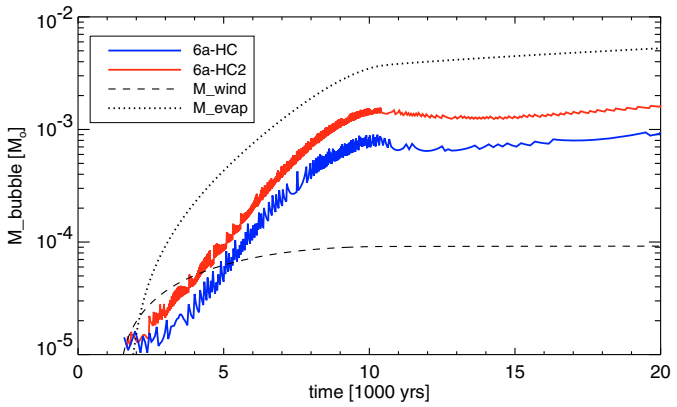

Fig. 6. Evolution of the bubble mass with time for the sequences Nos. 6a-HC and 6a-HC2. Gas hotter than 10^5 K is considered to belong to the bubble. The scatter is numerical noise. The dashed line indicates the mass blown into the bubble by the central-star wind, counted from t = 1200 yr. The dotted line gives a theoretical upper limit of the "evaporated" mass based on Eq. (16).

the "evaporated" nebular matter soon exceeds the matter blown into the bubble by the stellar wind. After 10 000 yr of evolution across the Hertzsprung-Russell diagram, the mass contained in the bubble reaches a maximum which depends on the treatment of thermal conduction: $\simeq 8 \times 10^{-4}$ $M_\odot$ (HC) and $\simeq 15 \times 10^{-4}$ $M_\odot$ (HC2), respectively, which is still negligible compared to a typical PN shell mass of about 0.1 $M_\odot$. Obviously, the reduced thermal conduction efficiency of method 1 results in a lower evaporation rate of cold gas relative to that of method 2. In either case, the whole bubble mass is virtually confined in a narrow outer shell.

Note that most of the mass blown-off by the central-star wind during the post-AGB evolution is not contained in the hot bubble but in the inner part of the nebula. The (reverse) wind shock forms only when the wind speed exceeds a certain value, which happens at about 1200 yr after departure from the tip of the AGB in the case of a 0.595 $M_\odot$ central-star model (for the zero point see Fig. 2). Only about 1×10^{-4} $M_\odot$ are blown into the bubble during the remaining part of evolution (Fig. 6).

The general time dependence of the bubble mass as shown in Fig. 6 can be interpreted in the following way. According to Borkowski et al. (1990), one can distinguish three different phases for thermal conduction fronts: (i) the "evaporation" phase in which the front advances relative to the initial interface and heats cool gas; (ii) the quasi-static phase in which the front stalls because heating and "evaporation" balance radiative cooling and "condensation"; (iii) the "condensation" phase in which the front recedes relative to the previous position because cooling/"condensation" dominates.

As long as the wind power and hence the energy input into the bubble increases steadily, the conduction front is obviously in the "evaporation" phase, and cooler nebular gas is heated and added to the bubble. This phase ends when the stellar luminosity, and hence also the wind power, drops because hydrogen burning ceases. This occurs in our simulations after about 10 000 yr of post-AGB evolution for the 0.595 $M_\odot$ model shown in Fig. 6 (see also bottom left panel of Fig. 2). For the following ≈3500 yr radiation cooling dominates, and the front becomes "condensation" dominated, leading to a small reduction of the bubble mass (Fig. 6) and the rate of expansion. After the rapid fading of the central star has stopped at about 12 000 yr, the wind is blowing with nearly constant albeit lower strength (Fig. 2). Due to the continued expansion, densities decrease and radiative losses becomes less important; the conduction front turns slowly back into the "evaporating" stage, and the bubble mass starts to increase again, but at a reduced rate (Fig. 6).

For spherical cases Weaver et al. (1977) estimated analytically an evaporation rate of

$$\begin{aligned} \dot{M}_{\rm hb} &= C_1 \langle T_{\rm hb} \rangle^{5/2} R_{\rm hb}^2 / (R_{\rm hb} - R_{\rm s}) \\ &\simeq C_1 \langle T_{\rm hb} \rangle^{5/2} R_{\rm hb} \quad \text{since} \quad R_{\rm s} \ll R_{\rm hb}\,, \end{aligned} \tag{9}$$

where $C_1 \approx 4.13{\times}10^{-14}$ and $\langle T_{\rm hb} \rangle$, $R_{\rm hb}$, and $R_{\rm s}$ are the mean temperature of the hot bubble, its radial size, and the position of the wind shock, respectively. The central star defines the origin, and the wind shock at $R_{\rm s}$ constitutes the inner boundary of the bubble. It must be noted, however, that Eq. (9) assumes that radiative cooling of the bubble is negligible, and thus provides only an upper limit of the evaporation rate (cf. Weaver et al. 1977, Eq. (61) therein).

Equation (9) allows us to compute the (equilibrium) evaporation rate of a bubble with given temperature and radius. However, what we really want to know here is how the mean temperature of the hot bubble, and hence its evaporation rate, depend on the power of the stellar wind, $L_{\rm wind} = \dot{M}_{\rm wind} v_{\rm wind}^2 / 2$.

To answer this question, we consider the energy balance of the hot bubble, first without heat conduction. In this case, the kinetic energy of the stellar wind is used to increase the thermal and kinetic engery of the bubble, to cover the work done by the expansion of the bubble, and to compensate possible radiative losses from the bubble:

$$L_{\rm wind} = \dot{E}_{\rm th} + \dot{E}_{\rm kin} + W_{\rm exp} + Q_{\rm rad}, \tag{10}$$

where $Q_{\rm rad}$ represents the net radiative cooling rate integrated over the volume of the bubble. Denoting by $f_{\rm th}$ the fraction of the wind power that is converted into thermal energy, we can write

$$f_{\rm th}\, L_{\rm wind} = \dot{E}_{\rm th} = \dot{M}_{\rm wind}\, \frac{3}{2}\, \frac{k}{\mu}\, T_0, \tag{11}$$

where $\dot{M}_{\rm wind}$ is the stellar mass loss rate and T_0 the temperature of the shock-heated bubble. For a strong adiabatic shock, $f_{\rm th} = 9/16$ and T_0 is given by the relation

$$T_0 = \frac{3}{16}\, \frac{\mu}{k}\, v_{\rm wind}^2, \quad \text{or} \quad T_0 \approx 1.4 \times 10^7 \left(\frac{v_{\rm wind}}{1000\ {\rm km\ s^{-1}}}\right)^2\ [{\rm K}]. \tag{12}$$

Here $v_{\rm wind}$ is the velocity of the stellar wind, and μ is the average mass of the gas particles. The numerical factor in Eq. (12) was obtained assuming $\mu = 0.6\, m_{\rm H}$ for fully ionized plasma of solar composition. According to Eq. (12), the temperature of the hot bubble depends only on the wind velocity. We note that the bubble temperatures of the two models shown in Fig. 5 cannot be understood with this relation: the stellar wind of the more massive central star (top) is about two times slower than that of the less massive one (bottom), but its bubble temperature is about 3 times higher! Obviously, thermal conduction makes a difference.

In the presence of heat conduction, the mass of the of bubble increases both due to the mass loss through the stellar wind with rate $\dot{M}_{\rm wind}$, and due to "evaporation" through thermal conduction with rate $\dot{M}_{\rm hb}$. Under these circumstances, the wind must supply the power to heat and expand both the stellar wind entering the bubble through the inner shock and the mass being added at the surface of the bubble by "evaporation". The mean temperature of the bubble, $\langle T_{\rm hb}\rangle$, is then given by the relation

$$\begin{aligned} f_{\rm th}\, L_{\rm wind} = \dot{E}_{\rm th} &= \frac{3}{2}\, \frac{k}{\mu} \left(\dot{M}_{\rm wind} + \dot{M}_{\rm hb}\right) \langle T_{\rm hb}\rangle \\ &= \frac{3}{2}\, \frac{k}{\mu} \left(\dot{M}_{\rm wind}\, \langle T_{\rm hb}\rangle + C_1\, \langle T_{\rm hb}\rangle^{7/2}\, R_{\rm hb}\right), \end{aligned} \tag{13}$$

where we have used Eq. (9). Equation (13) can be used to estimate the mean temperature of the hot bubble for given wind power, wind mass loss rate, and bubble size. In turn, the evaporation rate follows from Eq. (9).

If $\dot{M}_{\rm wind} \ll \dot{M}_{\rm hb}$, which is a valid approximation during the main part of the evolution (once the bubble is well established until the central star begins to fade, see Figs. 6 and 8), we obtain

$$\langle T_{\rm hb}\rangle^{7/2} = \frac{f_{\rm th}\, L_{\rm wind}}{\left(\frac{3}{2}\frac{k}{\mu} C_1\, R_{\rm hb}\right)} \quad \text{or} \quad \langle T_{\rm hb}\rangle \approx 24 \left(\frac{L_{\rm wind}}{R_{\rm hb}}\right)^{2/7}. \tag{14}$$

According to Eq. (14), the temperature of the hot bubble depends on the wind power and the bubble radius. This relation explains the behavior of the two models shown in Fig. 5: the 3 times higher wind power of the more massive central star, and its 10 times smaller bubble size imply a mean bubble temperature which is about 2.6 times higher that that of the less massive model.

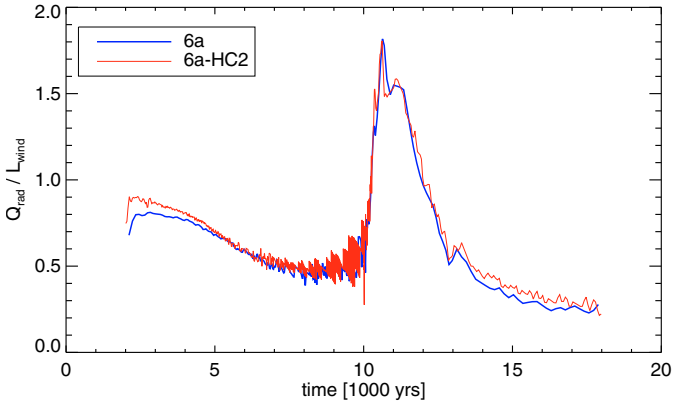

Fig. 7. The ratio $Q_{\rm rad}/L_{\rm wind}$ as a function of time for models 6a (thick) and 6a-HC2 (thin). Radiative losses are confined to a thin layer at the outer surface of the hot bubble; they are slightly larger in the presence of thermal conduction.

Combining Eqs. (9) and (14), we can write the evaporation rate as

$$\dot{M}_{\rm hb} = \frac{f_{\rm th}^{5/7}\, L_{\rm wind}^{5/7}\, C_1^{2/7}\, R_{\rm hb}^{2/7}}{\left(\frac{3}{2}\frac{k}{\mu}\right)^{5/7}} \tag{15}$$

or

$$\dot{M}_{\rm hb} = 1.3 \times 10^{-7} \left(\frac{L_{\rm wind}}{L_\odot}\right)^{5/7} \left(\frac{R_{\rm hb}}{10^{17}\ {\rm cm}}\right)^{2/7}\ [{\rm M_\odot\ yr^{-1}}]. \tag{16}$$

The dotted curves shown in Figs. 6 and 8 were obtained by integrating Eq. (16) over time, given $L_{\rm wind}(t)$ and $R_{\rm hb}(t)$ for the respective model sequence. Note again that Eq. (16) gives an upper limit of the evaporation rate, since both $f_{\rm th}$ and C_1 will be smaller than assumed here if radiation losses are important.

In our model simulations, "evaporation" due to thermal conduction is significantly less efficient than predicted by Eq. (16). As shown in Fig. 6, the mass of the hot bubble measured in the numerical model is a factor 3 to 5 lower than suggested by the analytical estimate. In-depth investigations have revealed that this discrepancy is caused by substantial radiative energy losses at the conduction front / contact discontinuity. As illustrated in Fig. 7, these losses are most severe in the early phases, when a large fraction of the wind power is radiated away. This explains also why the bubble mass grows very slowly at the beginning: a considerable part of the mass added to the bubble by the stellar wind cools efficiently and "condensates" outside the bubble. Later, "evaporation" becomes more efficient and the mass of the bubble grows much faster than implied by the wind moss loss rate. But even at $t = 8000$ yr, 50% of the wind power is still lost as radiation. It is interesting to note that the radiative cooling at the surface of the hot bubble is hardly altered by thermal conduction (see Fig. 7).

For completeness we show in Fig. 8 the evolution of bubble masses for two sequences with a more massive (0.696 $M_\odot$) and for one sequence with a less massive central star. The two sequences Nos. 10-HC2 and 10a-HC2 with the massive central-star model (top panel) differ only by their AGB mass-loss rates of 1×10^{-4} and 2×10^{-4} $M_\odot\ {\rm yr^{-1}}$, respectively (see Table 2).

For the 0.696 $M_\odot$ cases, the time evolution is similar as already discussed above for 0.595 $M_\odot$. A phase of rapidly increasing bubble mass is followed by a substantial decrease when the heat supply by the fading central-star wind drops. The "condensation" of bubble mass is more severe in the 0.696 $M_\odot$

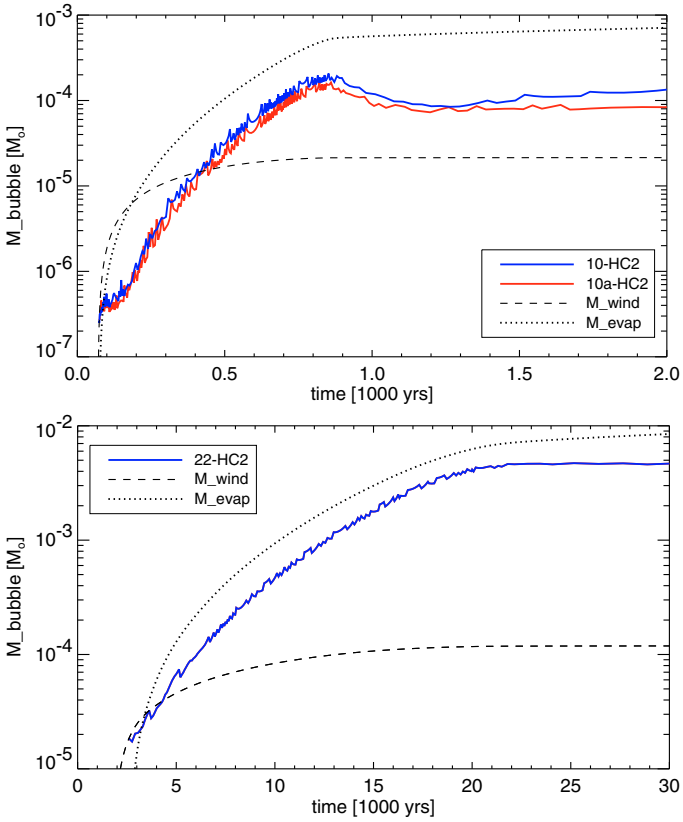

Fig. 8. The bubble masses vs. time for two sequences with a 0.696 $M_\odot$ central star (Nos. 10-HC2 and 10a-HC2) (*top*) and the 0.565 $M_\odot$ sequence (No. 22-HC2) (*bottom*). Again, only gas hotter than 10^5 K is considered to belong to the bubbles. The dashed line indicates the masses blown into the bubble by the central-star wind, counted from t = 75 yr (0.696 $M_\odot$) and t = 2600 yr (0.565 $M_\odot$), respectively. The dotted line gives the theoretical upper limit of the "evaporated" mass based on Eq. (16).

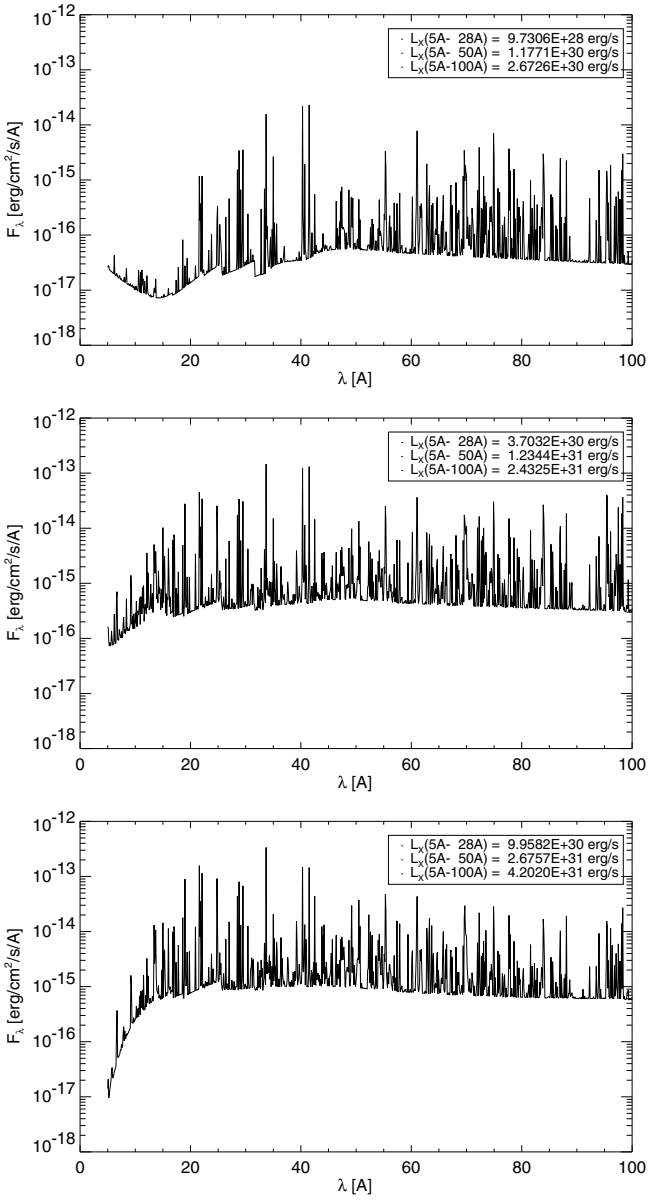

Fig. 9. The fluxes emitted in the wavelength band of 5−100 Å (2.5−0.125 keV) computed from the bubbles of the models shown in Fig. 4, without heat conduction (*top*), and with heat conduction included: HC (*middle*) and HC2 (*bottom*). The fluxes given in the ordinate refer to an assumed distance of 1 kpc, and the contribution of regions with $T_e < 10^5$ K is ignored. The insets give the luminosities in three different wavelength bands.

cases because the bubbles are small and rather dense ($n_e \approx 200 \ldots 500$ cm^{-3}), affording a more efficient radiative cooling. The discrepancy between the evaporation rate obtained from the simulation and the prediction of Eq. (16), respectively, is even more severe than in the case of the central star with 0.595 $M_\odot$.

Since the massive central-star models evolve on very short time scales, their bubbles are the smallest in size and mass of all sequences computed. The slightly smaller bubble masses found for sequence No. 10a-HC2 (as compared to those of sequence No. 10-HC2) are due to their somewhat smaller sizes, a consequence of the denser bubble environment caused by the larger AGB mass-loss rate, $\dot{M}_{\rm agb} = 2 \times 10^{-4}\ M_\odot\,{\rm yr}^{-1}$ instead of $\dot{M}_{\rm agb} = 1 \times 10^{-4}\ M_\odot\,{\rm yr}^{-1}$.

In the case of the low-mass central star (0.565 $M_\odot$), the wind power drops slowly after 20 000 yr of post-AGB evolution. As a result, the mass of the hot bubble ceases to increase. But in contrast to the simulations with more massive central stars, there is no real "condensation" phase. Rather, the mass of the hot bubble remains constant with time, obviously because radiative cooling is inefficient due to the low plasma densities. Hence, we find the best agreement between analytical and numerical evaporation rate for this sequence.

We finally note that "evaporation" due to heat conduction (HC2) increases the bubble mass by as much as a factor of 10, relative to the wind-blown mass, for the 0.696 $M_\odot$ cases, and by a factor of about 40 for the model with M = 0.565 $M_\odot$ near the end of the evolution (t > 20 000 yr), when "evaporation" and "condensation" balance and the bubble mass is essentially constant (see Fig. 8). The case of 0.595 $M_\odot$ is intermediate.

4. The X-ray emission

4.1. Spectra

We computed detailed X-ray spectra, as described in Sect. 2.3, for the wavelength interval 5−100 Å, corresponding to 2.5−0.125 keV. Examples are shown in Fig. 9 for the three models from Fig. 4. The X-ray emission consists of a continuum and numerous strong lines of highly ionized species. The models with thermal conduction included (middle and bottom panel of Fig. 9) have much larger fluxes in the 5−100 Å wavelength

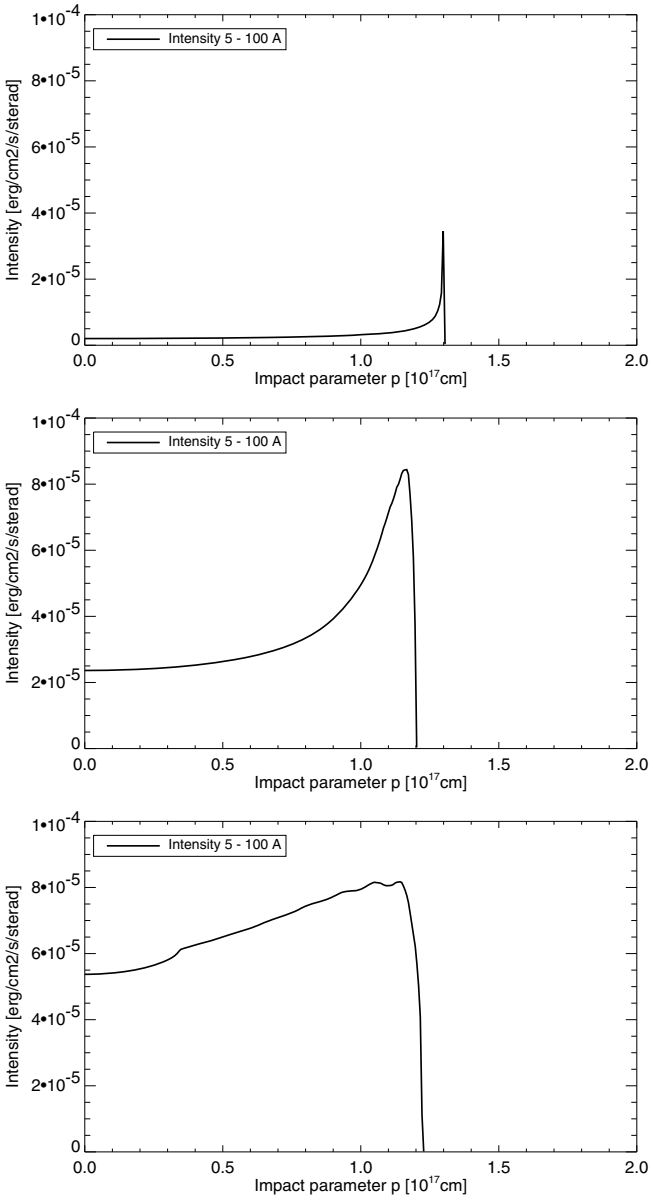

Fig. 10. Radial intensity profiles, integrated over the wavelength band of 5−100 Å (2.5–0.125 keV), of the models from Fig. 9 without (*top*) and with heat conduction considered: HC (*middle*) and HC2 (*bottom*). At impact parameter $p = 3.3\times10^{16}$ cm the inner edge of the bubble, i.e. the position of the (reverse) wind shock, is visible in *the bottom panel*.

band than the model without conduction. The total X-ray luminosities (in the same spectral band) are 2.4×10^{31} erg s^{-1} (HC) and 4.2×10^{31} erg s^{-1} (HC2), corresponding to $1.2\times10^{-6}\,L_{\rm star}$ (or $6.3\times10^{-3}\,L_\odot$) and $2.1\times10^{-6}\,L_{\rm star}$ (or $1.1\times10^{-2}\,L_\odot$), respectively. Without thermal conduction, the X-ray luminosity is only 2.7×10^{30} erg s^{-1} in the same wavelength band. In any case, these luminosities are only minute fractions of the mechanical energy carried away by the central-star wind, which is about 3.4 $L_\odot$ for the models used in Fig. 9 (cf. Fig. 2).

We note that our models with thermal conduction included provide X-ray luminosities which are smaller than those computed by Zhekov & Perinotto (1996) (by roughly a factor 10). However, radiative line cooling is not included in their analytical models, leading to a severe overestimation of the evaporation rate (see Sect. 3.3). Moreover, the simplified assumptions that only wind interaction is responsible for the compression of the AGB wind, ignoring the effects of photoionization, result in an unrealistic expansion behavior of the bubble.

We conclude that an approach like the one conducted by Zhekov & Perinotto (1996) is likely too simple for a reliable computation of the X-ray emission from planetary nebulae.

We emphasize in this context that the X-ray flux depends also on the chemical composition of the bubble gas. A detailed investigation of how the X-ray flux depends on the chemical composition, especially for cases with hydrogen-poor stellar winds, will be the subject of future work.

4.2. Surface brightness distributions

The X-ray intensity, integrated over the wavelength band of 5−100 Å, is limb-brightened and reflects the fact that the regions with physical properties favorable for emitting X-rays are mainly the outer layers of the hot bubble (Fig. 10). The absolute value of the intensity and its radial profile depend therefore sensitively on the way thermal conduction is treated.

In the case without any thermal conduction, the X-rays are emitted only from the very thin interface between the hot shocked stellar wind and the PN gas, resulting in a ring-like, comparatively weak emission (Fig. 10, top panel). In the case of low-efficiency heat conduction (method 1) the X-ray emission is still rather strongly peaked towards the bubble's surface, with a center-to-limb variation of a factor 4 (middle panel). Method 2 results in a more homogeneously distributed X-ray emission with a modest center-to-limb variation of only a factor 1.5. A larger part of the bubble is now contributing to the X-ray emission (bottom panel).

One notices that, although all the three models shown in Fig. 10 originated from the same initial configuration and are virtually of equal age, the sizes of their bubbles differ by a small amount: with thermal conduction included the bubble is a little bit smaller, $r_{\rm hb} = 1.2\times10^{17}$ cm instead of $r_{\rm hb} = 1.3\times10^{17}$ cm in the case without conduction[3]. This appears to be related to the fact that radiative energy losses from the bubble are somewhat larger for models including thermal conduction (see Fig. 7). This additional cooling causes a slightly slower expansion of the bubble, but is too small to significantly change the dynamics of the whole nebula: the PN evolution is virtually not influenced by heat conduction (cf. Fig. 4).

4.3. Time evolution

An important criterion for the usefulness of thermal conduction in explaining the X-ray emission from planetary nebulae is not only the predicted X-ray luminosity itself, but also how it evolves with time, i.e. as a function of the stellar parameters. In general, the X-ray luminosity is determined, for a given temperature, by the total volume emission measure of the X-ray emitting region, $\eta_{\rm X} \simeq \rho_{\rm X} M_{\rm X}$, with $\rho_{\rm X}$ being a characteristic mean density of the emitting volume and $M_{\rm X}$ its mass. For simplicity we set $\rho_{\rm X} \propto M_{\rm X}/R_{\rm hb}^3$. If $M_{\rm X} \propto t^a$ and $R_{\rm hb} \propto t^b$, we have $L_{\rm X} \propto \rho_{\rm X} M_{\rm X} \propto t^{2a-3b}$.

Considering for the moment no thermal conduction, and assuming a central-star wind with constant mass-loss rate and velocity, we have $a = 1$ and $b = 1$, where the latter expression holds if the bubble expands into an environment with $\rho \propto r^{-2}$ (Koo & McKee 1992, Eq. (3.1) therein). In this case, $L_{\rm X} \propto t^{-1}$ (see also Volk & Kwok 1985, Eq. (33)). This situation changes

[3] In the cases with heat conduction, the size of the bubble, $r_{\rm hb}$, is defined by the outer edge of the conduction front.

somewhat if the X-rays are only observed within a limited energy range and if the wind is evolving in time, i.e. if the wind speed increases (cf. Fig. 2). Since the post-shock temperature scales with wind speed squared, the X-ray emission increases first, reaches a maximum at an appropriate wind velocity, and drops then rapidly (see Volk & Kwok 1985, Figs. 11–13 therein). Note that in the case of increasing stellar wind power the bubble expansion is accelerated ($b > 1$), leading to a faster X-ray luminosity drop than in the case of a constant wind.

We have already seen in Sect. 3 that thermal conduction across the bubble/PN interface causes the bubble mass to increase rapidly with time thanks to "evaporation" from the dense nebular matter. For the case shown in Fig. 6, $a \simeq 4.5$ and $b \simeq 2$, leading to $L_X \propto t^3$. Any variation of T_X, the characteristic temperature of the X-ray emitting volume, during the course of evolution is thereby neglected.

This variation of the emission measure is the consequence of the adopted wind model in which wind power and speed increase during the evolution as shown in Fig. 2. Obviously the bubble mass increases faster by heat conduction than the density decreases by expansion. In contrast, the X-ray luminosity would increase only linearly with time if we assume $\dot{M}_{hb} \propto R_{hb}$ (Eq. (9)) and a linear expansion law, $R_{hb} \propto t$, instead.

According to the approximate expression for the emission measure given above, it is also possible that L_X decreases with time, provided $2a-3b$ becomes negative, or $a < 1.5\,b$, at some point during the evolution. This happens for instance in our simulations when the wind power decreases at the end of the evolution (a becomes even negative, cf. Figs. 6 and 8). Another possibility is a weak wind generating only a small evaporation rate.

The temporal evolution of the X-ray emission for a selection of our sequences listed in Table 2 is presented in Fig. 11. We consider only models computed with heat conduction according to method 2 (HC2). All sequences are plotted from the early transition phase until the white-dwarf domain is reached. Note that the evolutionary time scales decrease rapidly with stellar mass; it takes only ≃1000 yr for the 0.696 $M_\odot$ central star to exhaust its hydrogen-burning shell.

At first glance it appears to be astonishing that, according to our simulations, X-ray luminosities increase systematically with central-star mass, despite the fact that the bubble masses decrease (cf. Sect 3.3). This is, however, a consequence of the dependence of post-AGB evolution on central-star mass: both the stellar wind power and evolutionary speed increase substantially with remnant mass. As a result, the hot bubbles around more massive objects remain smaller and more dense and have larger emission measures despite of their smaller masses as compared to those around less massive and more slowly evolving central stars.

The trend of the X-ray emission with age is expected from the previous discussions. At early times, at the beginning of the sequences shown in Fig. 11, the X-ray luminosities increase sharply with time, reflecting the increase of wind speed and the resulting increase of post-shock temperatures to values suitable for soft X-ray emission (top panel). Note that both types of models, with and without heat conduction, give virtually the same X-ray emission during this phase, because the fraction of "evaporated" matter is still insignificant. This is typical for the "early-wind" phase of evolution when heat conduction is still unimportant.

For the energy range considered here (0.25–2.5 keV), there appears to be an optimum velocity, $v_{wind} \simeq 400$ km s^{-1} ($T_{post-shock} \simeq 2.3 \times 10^6$ K, see Eq. (12)) for which the X-ray

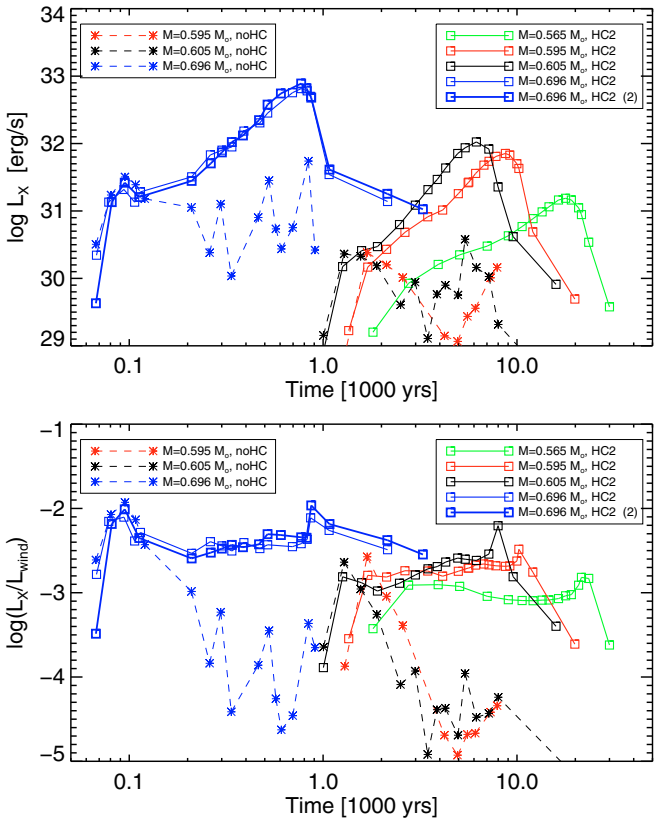

Fig. 11. Development of the X-ray luminosity in the wavelength range 5 to 50 Å (2.5–0.25 keV) as a function of time for the hydrodynamical sequences indicated in the inset. Five sequences have heat conduction included (22-HC2, 6a-HC2, 6-HC2, 10-HC2, and 10a-HC2 of Table 2), and three are without heat conduction for comparison (6a, 6, and 10, dashed). The strong fluctuation of X-ray luminosities of these models reflect the large numerical uncertainties related to the thinness of the X-ray emitting region. The symbols indicate the times at which the X-ray emission was computed by means of the CHIANTI code (cf. Sect. 2.3). The two panels show L_X vs. time (*top*) and L_X/L_{wind} vs. time (*bottom*), respectively.

emission of *models without thermal conduction* reaches a maximum. This happens at $t \simeq 95$ yr for the 0.696 $M_\odot$ sequence and $t \simeq 1800$ yr for 0.595 $M_\odot$, respectively, when the central stars are still very cool ($T_{eff} < 25\,000$ K) and the planetary nebula formation is just beginning. The luminosities achieved ($\simeq 10^{30}$–10^{31} erg s^{-1}) are in the observed range, but the stellar parameters like temperature and wind speed are inconsistent with the observed values! Beyond this maximum, the X-ray emission decreases with time due to expansion and because the bubble becomes too hot in the absence of heat conduction. The memory of the "early-wind" phase is lost.

The situation changes completely if heat conduction is included in the simulations. The X-ray luminosity increases with time to levels up to 2 dex *above* the values achieved without conduction. The trend with age is in line with the discussion above, i.e. an increase with time (or buble size) until the central star is rapidly fading (top panel of Fig. 11). This occurs after about 9000 yr of evolution for 0.595 $M_\odot$, after about 6000 yr for 0.605 $M_\odot$, and after only 800 yr for 0.696 $M_\odot$.

The final evolution, once the fading of the PN nucleus has stopped, is interesting. We see from Fig. 6 that the heat conduction turns back into the "evaporation" stage (at $t \simeq 15\,000$ yr for the $M = 0.595\,M_\odot$ example), albeit with much reduced efficiency. The "evaporated" nebular mass is, however, not sufficient

to compensate for the emission measure decrease due to expansion, and thus the X-ray luminosity decreases with time as well.

Altogether we see that the numerical simulations confirm the qualitative estimates made above: during the horizontal part of the evolution across the HR diagram the high evaporation rate triggered by a powerful and accelerating stellar wind dominates and leads to an ever increasing X-ray power. At the end of the evolution when the wind dies, the continued expansion reduces the emission measure for the X-rays.

Figure 11 demonstrates also the dependence of the X-ray luminosity on details of the final AGB mass-loss rate. First of all, the bubble of sequence No. 10-HC2 ($\dot{M}_{\rm agb} = 1 \times 10^{-4}\ M_\odot\,{\rm yr}^{-1}$) expands a little bit faster than that of sequence No. 10a-HC2 ($\dot{M}_{\rm agb} = 2 \times 10^{-4}\ M_\odot\,{\rm yr}^{-1}$) because the latter has a denser envelope. Consequently, they differ also somewhat in their X-ray luminosity. At the beginning of the evolution, the bubble of sequence No. 10a-HC2 with its denser shell develops a slightly lower X-ray luminosity because its emission measure $\rho_{\rm X} M_{\rm X}$ is lower: the smaller $M_{\rm X}$ is not adequately compensated for by a larger $\rho_{\rm X}$. Later on, the radius difference between both sequences becomes larger, and the X-ray emission from sequence No. 10a-HC2 exceeds that of sequence No. 10-HC2 because of the large radius dependence of $\eta_{\rm X}$.

Our detailed hydrodynamical treatment does not confirm the scaling law derived by Zhekov & Perinotto (1996) according to which $L_{\rm X} \propto \dot{M}_{\rm agb}^{0.75}$ for constant AGB wind speed and given age. This law predicts an X-ray luminosity for sequence No. 10a-HC2 ($\dot{M}_{\rm agb} = 2 \times 10^{-4}\ M_\odot\,{\rm yr}^{-1}$) which is larger than the X-ray luminosity of sequence No. 10-HC2 ($\dot{M}_{\rm agb} = 1 \times 10^{-4}\ M_\odot\,{\rm yr}^{-1}$) by 0.23 dex for the whole evolution (cf. also the previous discussion of this matter in Sect. 4.1). Our dependence is smaller and more complicated.

The bottom panel of Fig. 11 illustrates in detail how the X-ray luminosity depends on the central-star's wind power. In general, a fraction of between 0.01 and 0.001 of the wind power is radiated away by X-rays between 5 and 50 Å during the high-luminosity/high wind-power phase of evolution. These fractions become, of course, smaller (larger) if the wavelength band is reduced (increased). The variations of $L_{\rm X}/L_{\rm wind}$ along a sequence reflect the response of thermal conduction to the stellar wind evolution: after the early maximum of X-ray emission the ratio $L_{\rm X}/L_{\rm wind}$ decreases first because it needs some time for the conduction to "evaporate" sufficient nebular matter to compensate for the expansion based reduction of the emission measure ($\simeq \rho_{\rm X} M_{\rm X}$). Then the X-ray luminosity turns out to be fairly proportional to the wind power during the following evolution across the HR diagram. The sudden increase of $L_{\rm X}/L_{\rm wind}$ immediately before the stellar (wind) luminosity declines is due to the fact that "condensation" occurs on a longer time scale than the stellar (wind) luminosity drop.

Without heat conduction included, $L_{\rm X}/L_{\rm wind}$ becomes very small during the course of evolution, viz. $\simeq 10^{-4}$–10^{-5}. This fact demonstrates that thermal conduction by electrons across the contact surface is an efficient means to convert wind power into X-ray radiation for the whole lifetime of a PN!

There is an additional factor that influences the X-ray luminosity: the spectral band used in the computations (and observations as well). Here it is the low energy limit that matters, since energies higher than $E \approx 0.65$ keV ($\lambda < 20$ Å) contribute very little to X-ray luminosity. Defining the X-ray band by 0.25 keV $< E <$ 2.5 keV (5 Å $< \lambda <$ 50 Å), more massive and luminous central stars show an apparently larger efficiency of converting wind power into X-ray power, as is clearly seen in Fig. 11. Defining instead the X-ray band by 0.05 keV $< E <$ 2.5 keV (5 Å $< \lambda <$ 250 Å), the ratio $L_{\rm X}/L_{\rm wind}$ becomes roughly 0.01 for the whole range of central star masses.

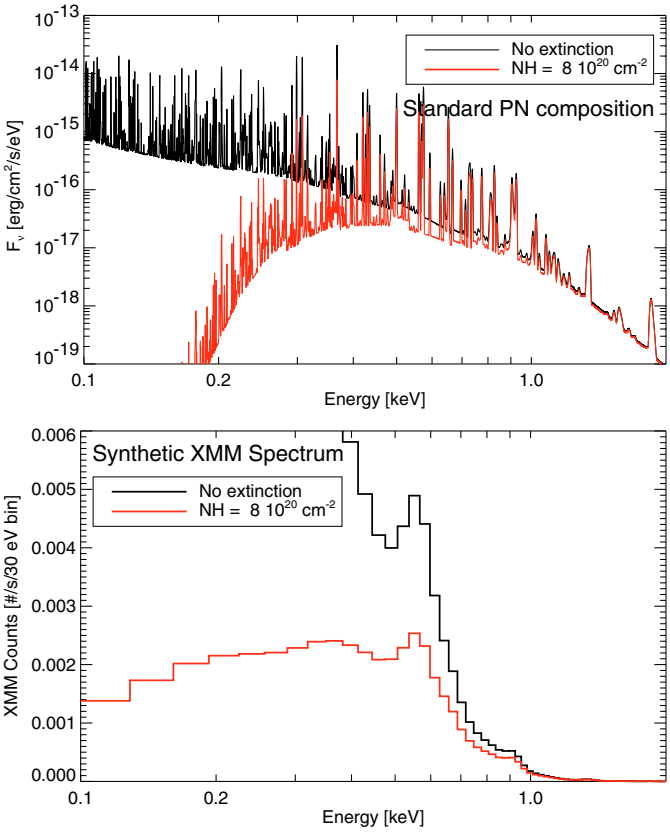

Fig. 12. *Top*: spectral flux densities computed from the model shown in the bottom panel of Fig. 4 (sequence No. 6a-HC2) at a distance of 1 kpc, non-attenuated (black) and attenuated by an intervening hydrogen column density of $N_{\rm H} = 8 \times 10^{20}$ cm^{-2} (grey). *Bottom*: simulated count rates per spectral bin of 0.03 keV width for the EPIC camera of the XMM-Newton satellite, with (gray) and without (black) absorption.

5. Comparison with observations

In this section we will compare the results of our thermal conduction simulations with existing observations from the X-ray satellites XMM-Newton and Chandra. Such a comparison is, however, extremely hampered by the fact that especially the soft X-ray emission is heavily absorbed by the interstellar medium. Another shortcoming of existing X-ray observations is their rather low spectral resolution.

As an example, Fig. 12 gives the computed X-ray flux from a nebular model as seen from a distance of 1 kpc, with and without interstellar absorption. The model used here is the one shown in the bottom panel of Fig. 4. It is of intermediate age, 5640 yr, and with stellar parameters of $M = 0.595\ M_\odot$, $L \simeq 5200\ L_\odot$, and $T_{\rm eff} \simeq 71\,500$ K it is a typical representative of most objects with known X-ray emission. The X-ray spectrum is not expected to change much while the star evolves across the HR diagram since the characteristic temperature of the X-ray emitting region remains rather constant during the high-luminosity part of evolution (cf. Fig. 18 in Sect. 5.2).

The upper panel of Fig. 12 demonstrates the effect of (interstellar) extinction on the fully resolved X-ray spectrum, assuming a column density of 8×10^{20} hydrogen atoms per cm^2.

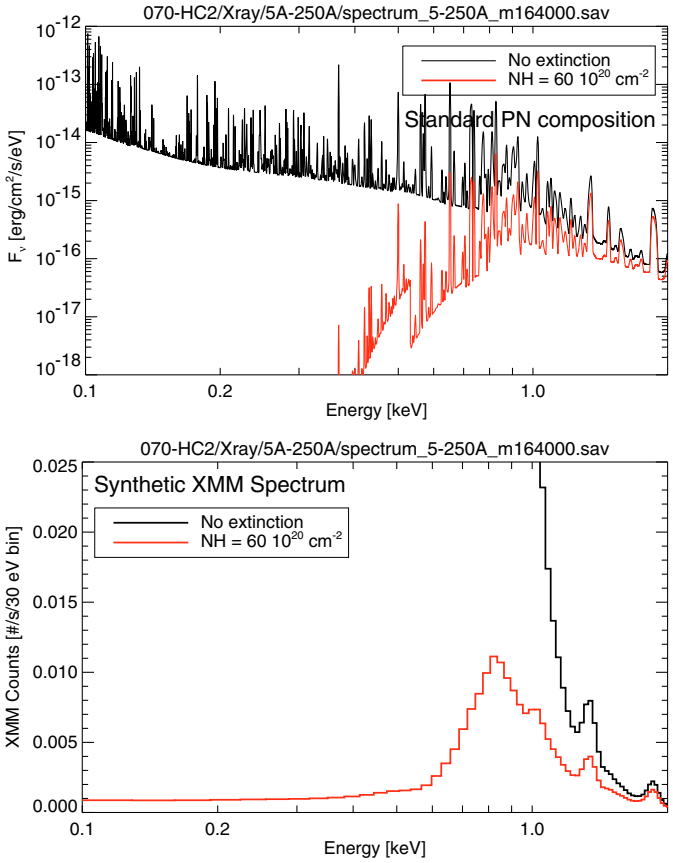

Fig. 13. *Top*: spectral flux densities computed from a model selected from sequence No. 10a-HC2 at a distance of 1 kpc, non-attenuated (black) and attenuated by an intervening hydrogen column density of $N_{\rm H} = 6 \times 10^{21}$ cm^{-2} (grey). The stellar parameters are: $M = 0.696\ M_\odot$, $L = 8403\ L_\odot$, $T_{\rm eff} = 199\,064$ K, $t = 695$ yr. *Bottom*: corresponding simulated count rates per spectral bin of 0.03 keV width for the EPIC camera of the XMM-Newton satellite, with (gray) and without (black) absorption.

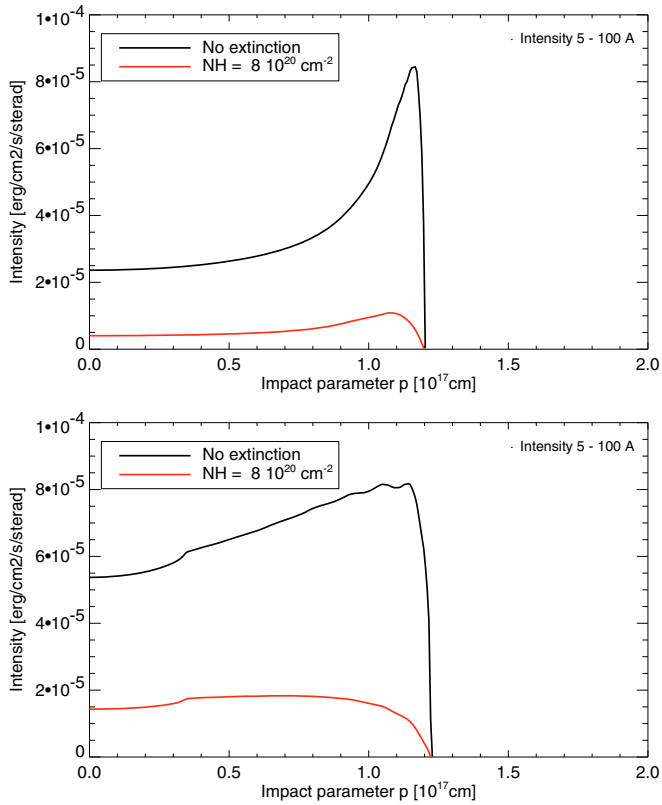

Fig. 14. *Top*: intensity profiles from Fig. 10, *middle panel*, subject to an absorption corresponding to a hydrogen column density of $N_{\rm H} = 8 \times 10^{20}$ cm^{-2} (grey). *Bottom*: the same for the *bottom panel* of Fig. 10. The black lines represent in both panels the unattenuated intensities. All intensities are integrated from 5–100 Å, corresponding to 2.5–0.125 keV.

The extinction cross section per hydrogen atom as a function of X-ray energy was calculated according to Morrison & McCammon (1983, Table 2). In the lower panel we show a simulation of the expected count rates as they would be measured by the XMM-Newton satellite with its limited spectral resolution, using an appropriate response matrix[4] describing the complex response of the energy channels of the EPIC camera to irradiation by X-ray photons of given energy. For comparison with published X-ray spectra of PNe, we have re-binned the XMM energy channels such that the full energy resolution of 5 eV is reduced to 30 eV. At this resolution, the only prominent feature seen at ≈0.55 keV (22 Å) belongs to the strong O VII complex. Other line features cannot be seen.

A second example is shown in Fig. 13 where the X-ray emission was computed for a model from sequence No. 10a-HC2 with $M = 0.696\ M_\odot$, and $L \approx 8400\ L_\odot$, $T_{\rm eff} \approx 200\,000$ K, representative of, e.g., NGC 7027. There is more flux at high energies as compared to the case in Fig. 12 because the bubble gas is now hotter (cf. Fig. 5, top).

According to Kastner et al. (2001), the absorption towards NGC 7027 is very high, $N_{\rm H} \approx 6 \times 10^{21}$ cm^{-2}, shifting the maximum of the *observed* X-ray emission to higher energies (bottom panel of Fig. 13). Our simulated XMM-Newton spectrum is very similar to that of NGC 7027 observed by the Chandra X-Ray Observatory (cf. Kastner et al. 2001): the maximum flux occurs between 0.8 and 0.9 keV, probably due to the Ne IX complex. Indeed, by looking at the top panel of Fig. 13 one sees a strong line blend around 0.9 keV (Ne IX) just at the maximum of the reddened flux density distribution. Ne IX is also strong for the model shown in Fig. 12, but far away from the maximum of the (reddened) flux density distribution. Because of the larger bubble temperature we see also peaks generated by Mg XI (≃1.3 keV) and Si XIII (≃1.9 keV). The O VII complex which is dominant at lower temperatures (cf. Fig. 12), is not visible anymore at this spectral resolution[5].

We see from these examples that the flux detectable from PNe is quite limited to a certain energy range: at high energies, the flux decreases due to the physical structure of the bubble, and at low energies the emission is heavily absorbed by the intervening interstellar matter, and possibly also by dust and neutral gas in and around the PN itself. The range useful for detecting X-rays appears to be between ≈0.2 and 2 keV (corresponding to the wavelength range 6 . . . 60 Å).

5.1. Absorbed X-ray surface brightness distributions

We have already discussed the intensity distributions of the X-rays emitted from PNe bubbles which are subjected to different treatments of the heat conduction in Sect. 4.2. Like the

[4] http://xmm.vilspa.esa.es/external/xmm_sw_cal/calib/epic_files.shtml

[5] Note that all the computations presented in this work were performed with the same chemical abundances, viz. those listed in Table 1.

Table 3. Relevant parameters of objects with detected X-ray emission. The luminosity, L_X, in the wavelength band 5−28 Å (0.45−2.5 keV), corrected for extinction and adjusted according to the distances used here, and typical values of temperature, T_X, and pressure, P_X, of the X-ray emitting volume as determined by Guerrero et al. (2005a). The effective temperatures are either spectroscopically derived (Méndez et al. 1992) or He II Zanstra temperatures (NGC 6543 and NGC 7027: Górny, priv. comm.). The distances are either spectroscopic ones (NGC 2392 and NGC 3242: Pauldrach et al. 2004) or based on expansion parallaxes (NGC 6543: Reed et al. 1999; NGC 7027: Schönberner et al. 2005a). The distance of NGC 7009 is again from Górny (priv. comm.). References for the central-star wind data: (1) Pauldrach et al. (2004); (2) Tinkler & Lamers (2002, Table 1 therein); (3) Georgiev et al. (2008, Table 1 therein). All objects listed in this table have central stars with normal, i.e. hydrogen-rich, composition.

Object	$T_{\rm eff}$ (K)	Distance (kpc)	$L_{\rm star}$ ($L_\odot$)	$\log L_X$ (erg s^{-1})	T_X (K)	P_X (dyne cm^{-2})	$\log(L_X/L_{\rm star})$	$\log \dot{M}_{\rm wind}$ ($M_\odot$ yr^{-1})	$v_{\rm wind}$ (km s^{-1})	$L_{\rm wind}$ ($L_\odot$)	$\log(L_X/L_{\rm wind})$	Ref.
NGC 2392	40 000	1.67	5010	31.20	2.0×10^6	2.6×10^{-8}	−6.09	−7.74	420	0.26	−1.81	(1)
NGC 3242	76 000	1.10	3120	30.90	2.2×10^6	7.6×10^{-9}	−6.18	−8.40	2400	1.89	−2.96	(1)
NGC 6543	67 000	1.00	1590	31.00	1.7×10^6	1.8×10^{-8}	−5.78	−7.73	1340	2.75	−3.01	(3)
NGC 7009	81 000	1.50	3600	31.34	1.8×10^6	1.4×10^{-8}	−5.80	−8.55	2770	1.78	−2.49	(2)
NGC 7027	200 000	0.80	6250	31.12	7.9×10^6	1.3×10^{-7}	−6.26	–	–	–	–	

spectral energy distribution, also the radial intensity distribution is expected to depend on absorption. The reason is the large variation of the absorption with frequency (see Figs. 12 and 13). The emission from the cooler, denser bubble gas is more heavily absorbed than that from the hotter but less dense gas further inwards. Consequently, the emission is weighted towards the hotter, less dense inner regions of the bubble.

This effect is illustrated in Fig. 14 where we show examples of radial X-ray intensity profiles with and without extinction for our two treatments of heat conduction. In both cases the centre-to-limb variation is considerably reduced if interstellar extinction is applied, and the maximum emission is shifted inwards. With method 2 the X-ray intensity appears to fill the region inside the nebular rim nearly homogeneously.

The radial distribution of the X-ray intensity offers obviously a possibility to put constraints on the physics of thermal conduction in very rarefied plasmas. Although it is difficult to estimate a definitive amount of center-to-limb variations from the existing X-ray maps, we note that the recent XMM-Newton observations of NGC 3242 presented by Ruiz et al. (2006) show a smooth distribution of X-ray emission with no apparent limb brightening. Thus we are inclined to conclude that our method 2 (labeled HC2) appears to be more appropriate to describe heat conduction in PNe. We will therefore discuss in the following sections only this case.

Although limb brightening is not really detectable, it is obvious that the X-ray intensity is often not homogeneously distributed across the bubble. In the heat conduction model this would be an indication that the conduction efficiency is not the same in all directions, maybe due to the presence of small-scale magnetic fields. It appears more likely, however, that the brightness variations are caused by non-uniform (intra-nebular/interstellar) extinction across the nebula (see discussion in Kastner et al. 2002), as found for many PNe in the visual wavelength range (e.g. Tsamis et al. 2008; Sandin et al. 2008).

5.2. X-ray luminosities

Now we compare global X-ray properties, in particular the luminosities, predicted by our models with the recent observations made by the Chandra and XMM-Newton satellites. We discarded objects with a WC central star because wind and hot bubble have a hydrogen-poor composition which is completely different from the (hydrogen-rich) composition assumed in our hydrodynamical simulations. The X-ray properties of the remaining five objects are listed in Table 3 and are taken from the compilation of Guerrero et al. (2005a) in order to have a homogeneous data set to compare with. Note that now the X-ray luminosities refer to the energy interval of 0.45−2.5 keV (5−28 Å) only in order to avoid large and uncertain corrections due to interstellar absorption at lower energies. The low energy cut-off used here leads to X-ray luminosities that are, in some cases, considerably *lower* than those quoted in the discovery papers. Additional changes are due to the adjusted distances used in our work. The X-ray data from the PNe are supplemented by the corresponding data of the stellar winds if available.

The empirical data of Table 3 allow already some interesting conclusions: Compared with the stellar luminosity, the X-ray contribution from the shocked stellar wind (i.e. from the bubble), for the energy band considered here, is very small and is only about $10^{-6}\,L_{\rm star}$. Also the fraction of the stellar wind power that is converted into X-ray emission is quite small: only 1% to 0.01%. Note that these values depend on the definition of the energy band, notably on the boundary of the low-energy region where most of the X-rays are emitted (see Fig. 9).

We present in the following figures a detailed comparison of the objects listed in Table 3 with the predictions of our hydrodynamical models with heat conduction treated according to method 2. We begin with the "X-ray Hertzsprung-Russell diagram" of Fig. 15, where we present the general evolution of the bubble's X-ray luminosity as a function of the stellar effective temperature for sequences with different central stars. The increase of the X-ray luminosities with time seen in Fig. 11 translates into a corresponding increase with effective temperature.

Given the distance uncertainty to individual objects, the agreement of our models with the existing observations is very good. The X-ray luminosity of all five objects from Table 3 can be explained by sequences with central stars between 0.6 and 0.7 $M_\odot$! We repeat that the run of the X-ray emission with time (or stellar effective temperature) depends on the stellar wind properties and the expansion rate of the bubble, which also depends indirectly on the wind. The evolution of the X-ray luminosity as seen in Fig. 15 is the result of the wind model shown in Fig. 2 (0.595 $M_\odot$). The sample of PNe with confirmed soft X-ray emission is, however, too small to prove or disprove the wind model used in our simulations.

Our models without thermal conduction fail completely in explaining the observations because their X-ray luminosities are too low by about two orders-of-magnitude at the positions of the observed objects in Fig. 15 (cf. also Fig. 11).

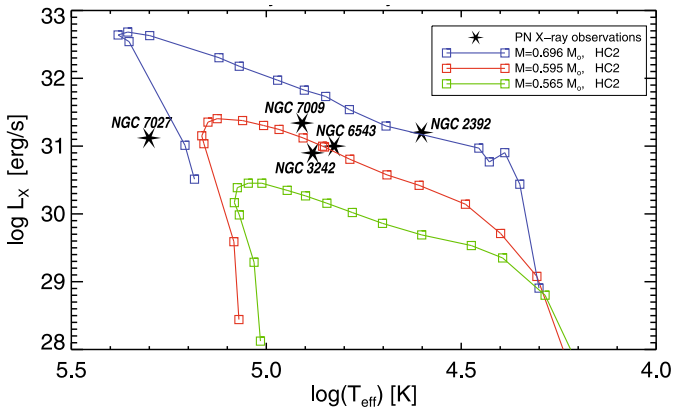

Fig. 15. X-ray luminosity of the bubble for the energy interval 0.45−2.5 keV (5−28 Å) as a function of the stellar effective temperature as predicted by three model sequences with central star masses 0.565 $M_\odot$, 0.595 $M_\odot$, and 0.696 $M_\odot$ (HC2 models only, see inset). The star symbols indicate the positions of the objects from Table 3. The evolution times covered by the model sequences are the same as in Fig. 11.

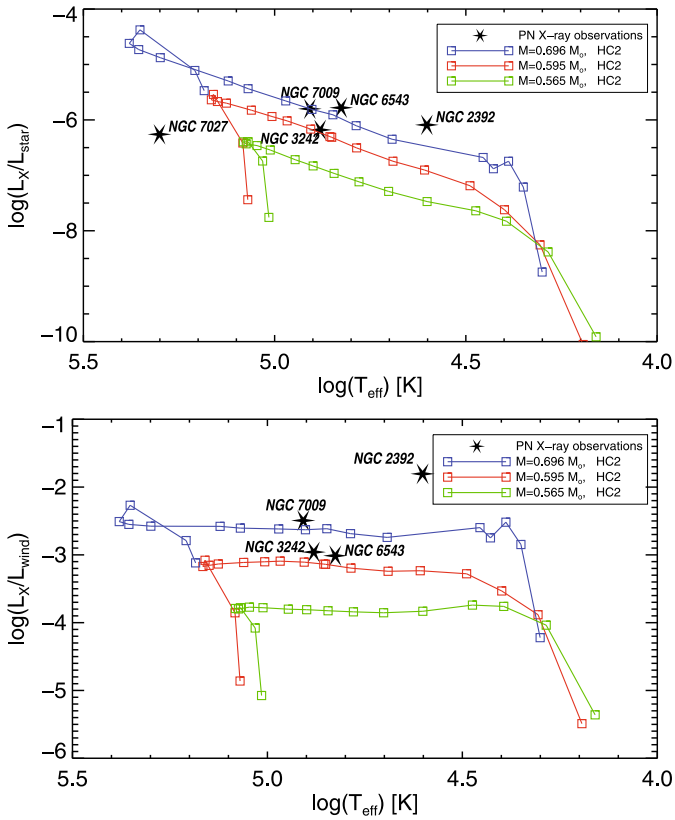

Fig. 16. *Top*: X-ray luminosity of the bubble (0.45−2.5 keV) over stellar luminosity vs. effective temperature. The model sequences are the same as in Fig. 15 (see inset). *Bottom*: X-ray luminosity of the bubble (0.45−2.5 keV) over stellar wind power vs. stellar effective temperature. The observations from Table 3 are again plotted as stars. Note that NGC 7027 cannot be shown in the bottom panel because its stellar wind properties are unknown.

In order to avoid possible systematic errors caused by distance uncertainties we relate in Fig. 16 the X-ray luminosities to both the stellar luminosity, L_X/L_{star}, and wind luminosity, L_X/L_{wind}. The basic result found from Fig. 15 is confirmed in Fig. 16 (top panel): our models with thermal conduction according to method 2 (HC2 models) predict soft X-ray emission in good agreement with the observations (except for NGC 7027, see discussion below). There appears to be a slight preference for our 0.7 $M_\odot$ models, but considering the uncertainties of L_X we don't think that this is a real effect.

The lower panel of Fig. 16 corresponds to that shown in the bottom panel of Fig. 11, although the difference between the tracks appears somewhat larger. The reason is the smaller energy range considered: the temperature sensitive emission at the high energy end has now more weight. Again we have a satisfactory agreement between theory and observations. Less than 1% of the wind power is converted into X-ray emission. Note, however, that the mass-loss rates which enter into the wind power are notoriously uncertain and may vary by up to a factor of ten between different authors!

As mentioned above, NGC 2392 has an unusually slow wind for its position in the Hertzsprung-Russell diagram compared with the other objects listed in Table 3, giving it the lowest wind luminosity and thus the highest L_X/L_{wind} ratio of all objects from the sample. Its X-ray luminosity agrees with our models (cf. Fig. 16, top), but its wind power is too small, and hence L_X/L_{wind} too large (cf. Fig. 16, bottom). It appears possible that fast outflows/jets contribute to the X-ray emission of NGC 2392 (see discussion in Guerrero et al. 2005b).

A further interesting comparison is shown in Fig. 17 where L_X/L_{star} is plotted over v_{wind}. This figure demonstrates clearly that our models, thanks to the inclusion of heat conduction, give a fully consistent description of the *observed* X-ray luminosities also in terms of the *observed* large wind speeds! Although the wind of NGC 7027 is not known, it must exist because we observe the X-ray emission from the shocked wind gas. Judging from the central star's position close to the white dwarf domain, we estimate a wind speed close to the right boundary of Fig. 17, viz. of about 7000 . . . 8000 km s^{-1}.

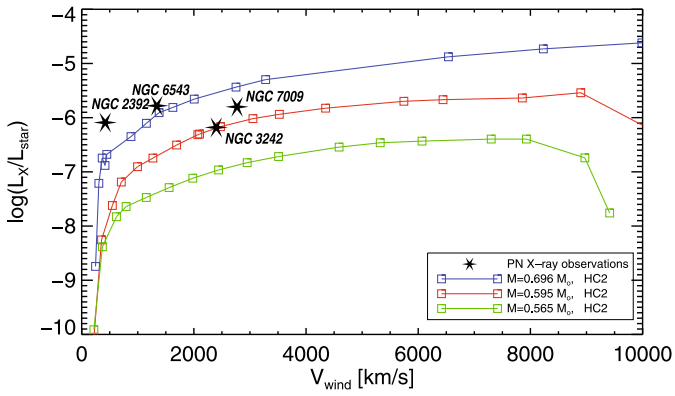

Fig. 17. L_X/L_{star} vs. wind speed, again for our three model sequences from Fig. 15 and the objects from Table 3 (except for NGC 7027 for which the central star wind is not known). The X-ray range is again 0.45−2.5 keV.

5.3. X-ray temperatures

A stringent test of our models is the determination of a characteristic X-ray emission temperature, T_X, which can be compared with the measurements. We computed T_X from our models by weighting the electron temperature $T_e(r)$ within the bubble

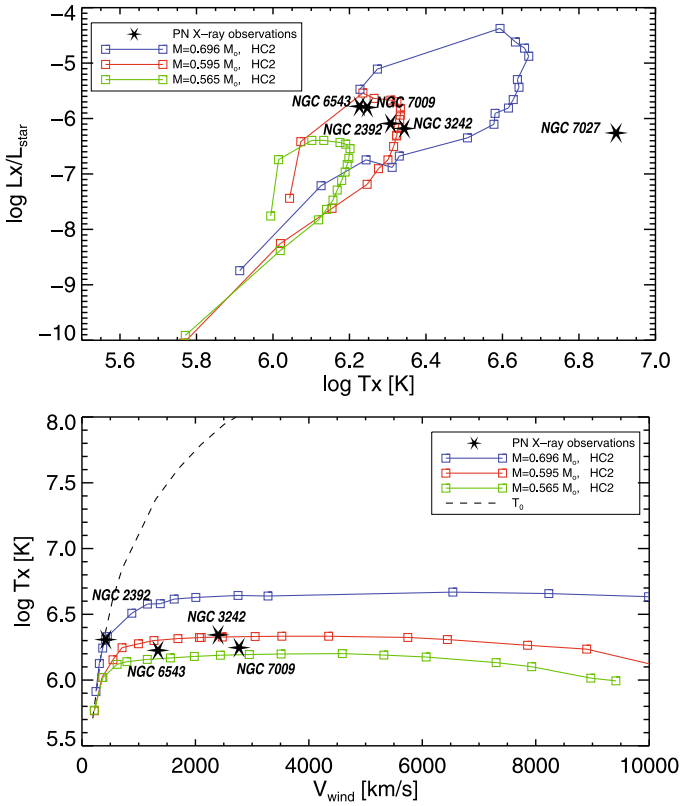

Fig. 18. *Top*: L_X/L_{star} for the 0.45−2.5 keV range as a function of the characteristic temperature of the X-ray emitting region, T_X, again for the three sequences from Fig. 15. The individual "tracks" cover the same age spans as shown in Fig. 11. Note that the observed values of T_X (from Table 3) have been derived from the best fit to the spectral energy distributions, while the T_X for a given hydrodynamical model have been computed according to Eq. (17). *Bottom*: T_X as a function of the wind speed, v_{wind}, computed for the three model sequences from Fig. 15, and T_0 according to Eq. (12) (dashed).

(r_1-r_2) with the volume emissivity integrated over the respective energy range, $E_1 - E_2$ (0.45−2.5 keV or 5−28 Å):

$$T_X = \frac{4\pi}{L_X} \int_{r_1}^{r_2} r^2\, T_e(r)\, \eta_X(r)\, dr, \tag{17}$$

where L_X is the X-ray luminosity,

$$L_X = 4\pi \int_{r_1}^{r_2} r^2\, \eta_X(r)\, dr, \tag{18}$$

and

$$\eta_X(r) = \int_{E_1}^{E_2} \eta(T_e(r), n_e(r), E)\, dE, \tag{19}$$

is the volume emissivity in the energy band $E_1 - E_2$.

The result is seen in Fig. 18 (top panel), covering the whole evolution from the onset of the bubble formation until the white dwarf stage is reached (cf. Fig. 11). In general, T_X increases rapidly to above 10^6 K while a hot bubble is formed beyond the wind shock. Then heat conduction becomes effective, and T_X increases only slowly or remains nearly constant until maximum wind power is reached. This refers mainly to the "evaporation" phase during which the the conduction front advances outwards (see Sect. 3). Afterwards, T_X drops in line with the wind power to about 10^6 K ("condensation" phase).

The maximum X-ray temperature achieved during the evolution across the HR diagram depends on the central star mass: thanks to its powerful wind, the sequence with the 0.696 $M_\odot$ model reaches a much larger T_X than the sequence with the 0.565 $M_\odot$ star, viz. 4.5×10^6 K instead of only 1.6×10^6 K.

Assuming that our computed characteristic X-ray temperatures are reasonable representatives of the ones derived from observations, we find excellent agreement between theory and observations, except for NGC 7027 whose T_X (8×10^6 K) is much larger than our models predict (see also below). The remaining objects are rather well matched by the 0.595 $M_\odot$ models with heat conduction (sequence No. 6a-HC2).

The bottom panel of Fig. 18 illustrates how the temperature of the X-ray emitting region is modified by thermal conduction from a value close to the one predicted by Eq. (12). At very low wind speeds, typical for the "early-wind" phase, thermal conduction is unimportant, and T_X equals the post-shock temperature (dashed line in the bottom panel of Fig. 18). At faster stellar winds (and larger post-shock temperatures), T_X levels off as a consequence of heat conduction and becomes fairly independent of the wind speed.

5.4. Correlations with bubble radius

For a given central star mass, our models predict an increase of the X-ray luminosity with time (bubble radius) during the main phase of evolution (see Sect. 4.3, Fig. 11, top). On the other hand, the same models predict a decrease of L_X with bubble radius at given central star effective temperature. This is because, for given T_{eff}, L_X increases with stellar mass (see Sect. 5.2, Fig. 15), while the bubble size decreases due to the shorter evolution time scales of the more massive stars. Likewise, in the presence of heat conduction the mean temperature of the hot bubble ($\sim T_X$) depends on both the wind power and the bubble radius according to Eq. (14), but the dependence is weak. Hence, the expected correlations of L_X and T_X with bubble radius R_{hb} depend critically on the mass distribution and ages of the observed objects.

In this context we have to discuss the recent findings by Kastner et al. (2008) that X-ray temperature and luminosity appear to *decrease* with bubble radius. Apart from the fact that these results suffer from uncertainties of the distances of the individual objects, which the authors do not consider at all, we point out that:

1. Figure 4 of Kastner et al. (2008) contains a mix of objects: 4 PNe have hydrogen-deficient and 3 PNe have hydrogen-rich central stars. The objects from both groups have certainly *per se* distinct physical properties and also different evolutionary histories.
2. The 3 objects with a hydrogen-rich central star (NGC 2392, NGC 6543, NGC 7009) have about the same bubble radius of ∼0.1 pc.

The claimed anti-correlations with bubble radius are thus probably purely artificial, based entirely on an inappropriate combination of objects with different evolutionary background. A much larger, homogeneous sample of objects is certainly necessary to construct trustworthy correlations between observable quantities that can be compared with theoretical predictions.

5.5. Individual objects

NGC 3242. This PN is well suited for a closer comparison with our models because its bubble is most likely spherical, as

Table 4. Relevant parameters of two nebular models along the 0.595 $M_\odot$ track (sequence No. 6a-HC2) embracing the position of NGC 3242 in the HR diagram, compared with the observed properties of NGC 3242. For both observation and models, the X-ray data refer to the 0.45−2.5 keV energy band.

	Model 1	Model 2	NGC 3242	Ref.
$M/M_\odot$	0.595	0.595	0.53, 0.63	(1), (2)
$L_{\rm star}/L_\odot$	5205	5051	3162	(1)
$T_{\rm eff}$ (K)	71 667	80 457	75 000	(1)
$t_{\rm post-agb}$ (yr)	5 642	6 121	≃2800	(3)
$\dot{M}_{\rm wind}$ ($M_\odot$ yr^{-1})	9.7×10^{-9}	8.6×10^{-9}	4×10^{-9}	(1)
$v_{\rm wind}$ (km s^{-1})	2115	2490	2400	(1)
$L_{\rm X}/L_{\rm star}$	5.0×10^{-7}	6.8×10^{-7}	6.6×10^{-7}	Table 3
$L_{\rm X}/L_{\rm wind}$	7.2×10^{-4}	7.7×10^{-4}	1.1×10^{-3}	Table 3
$T_{\rm X}$ (K)	2.1×10^{6}	2.1×10^{6}	2.2×10^{6}	(4)
$P_{\rm X}$ (dyn cm^{-2})	9.0×10^{-9}	8.0×10^{-9}	7.6×10^{-9}	(4)
$P_{\rm rim}$ (dyn cm^{-2})	$\simeq8\times10^{-9}$	$\simeq7\times10^{-9}$	8.6×10^{-9}	(4)
$n_{\rm rim}$ (cm^{-3})	≃2900	≃2400	2600	(4)
$n_{\rm shell}$ (cm^{-3})	≃1200	≃800	800	(4)
$v_{\rm rim}$ (km s^{-1})	14.0	14.5	19.5	(5)
$v_{\rm shell}$ (km s^{-1})	27.0	28.0	35.7	(5)

(1) Pauldrach et al. (2004).
(2) Kudritzki et al. (2006).
(3) Kinematic age from Corradi et al. (2003), scaled down to the distance of 1.1 kpc used here.
(4) Ruiz et al. (2006).
(5) Schönberner et al. (2005b).

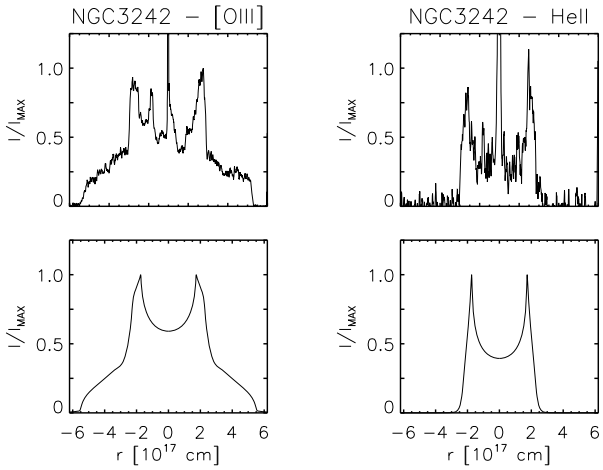

Fig. 19. *Top*: normalised intensity distributions of NGC 3242 in [O III] and He II from HST monochromatic images (F502N and F469N, respectively). The cuts are taken along the minor axes and scaled to the model sizes. The spikes at $r = 0$ are due to the central star. *Bottom*: normalised intensity distributions of an appropriate hydrodynamical model with a 0.595 $M_\odot$ central star that matches closely the observations for NGC 3242 (model 2 of Table 4).

judged from the ring-like appearance of the rim. The position of NGC 3242 is very close to the 0.595 $M_\odot$ track in all the previous figures (15−18). This implies that the evolution of wind power and X-ray emission as predicted by our model simulation with heat conduction according to method 2 reflects the real situation in NGC 3242 surprisingly well. A detailed comparison between the observed parameters of NGC 3242 and two models taken from sequence No. 6a-HC2 which embrace the observed position of NGC 3242 in the figures is presented in Table 4. The density and temperature structure of model 1 is shown in Fig. 4 (bottom panel).

Given the uncertainty of the observed data and the fact that we did not attempt to make any fits to the observations, the agreement is very good, especially for the X-ray related data. Notice the nearly equal pressures and temperatures of the X-ray emitting gas[6]. Also mass-loss rates and wind speeds are, within the known uncertainties, in reasonable agreement.

Quantities that depend directly on distance or distance squared differ by larger amounts. Our values for NGC 3242 quoted in Table 4 are based on a distance of 1.1 kpc, according to Pauldrach et al. (2004). Kudritzki et al. (2006) arrived at a larger distance, $d = 1.8$ kpc, hence luminosity and kinematic age are larger: $L = 7760\,L_\odot$ with an age of about 4600 yr[7]. These authors give also a larger mass-loss rate, $8\times10^{-9}\,M_\odot$ yr^{-1}, from the central star.

Taken at face values, the numbers listed in Table 4 indicate that the thermal pressure of the rim, $P_{\rm rim}$, exceeds that of the bubble by a small margin. In the model we have just the opposite situation. The case of NGC 3242 could thus indicate that the wind power of the central star has achieved its maximum value already below the present effective temperature of 75 000 K. This would be in line with the more recent wind computations conducted by Pauldrach et al. (2004) according to which central-star mass-loss rates and wind power reach a maximum around stellar temperatures of 50 000 K, after which the thermal pressure of the bubble drops below that of the rim (for more details see Steffen & Schönberner 2006, Fig. 6). In our present simulations which are based on the older Pauldrach et al. (1988) recommendations the wind power peaks later, close to maximum effective temperature (cf. Fig. 2, bottom left).

One may then ask whether also other structures of NGC 3242 are adequately represented by our models. First of all, the model has a dense rim and a large but less dense (attached) shell, and size and density ratios between rim and shell are about two and three, respectively. These values compare favorably with the observations, and also the (electron) densities are in good agreement: Ruiz et al. (2006) derived electron densities for NGC 3242 of 2600 cm^{-3} in the rim and 800 cm^{-3} in the shell, respectively (cf. Table 4).

Figure 19 gives a further illustration of the close relationship between NGC 3242 and our models: it shows the monochromatic brightness distributions in two important emission lines for NGC 3242 and for an appropriate model very close to the observed HRD position of NGC 3242. It is remarkable that also the ionization structure in both the real PN and the model is such that only the rim is doubly ionized in helium. Yet the model is not perfect: according to Table 4 the (spectroscopic) expansion velocities of rim and shell are lower than the observed ones. The velocity differences, however, are well matched.

NGC 7027. We note from Fig. 16 (top panel) that, although the X-ray luminosity of NGC 7027 compares well with those of the other objects shown in this figure, it is about 1.5 dex *below* the model prediction. Also, the X-ray emitting region is considerably hotter, viz. with 8×10^6 K about twice as hot as the maximum reached by our 0.696 $M_\odot$ models of sequence No. 10-HC2 (see Fig. 18). We have verified that NGC 7027

[6] The hot bubble is isobaric despite of the radial temperature and density gradients (cf. Fig. 4).
[7] Kinematic ages based on physical size and expansion velocity are problematic since they depend strongly on the method used (see Schönberner et al. 2005a). The relatively large shell expansion speed indicates a significant acceleration during the previous evolution which lead to an underestimation of the age.

is embraced by our sequences No. 10 (no conduction) and No. 10a-HC (method 1), so we conclude that thermal conduction may still work but at a lower level than our method 1 predicts. A possible solution would be the presence of a weak magnetic field which suppresses thermal conduction to some extent (cf. Borkowski et al. 1990).

Recently, Sabin et al. (2007) reported indeed the detection of polarization across NGC 7027 by means of SCUBA observations. The orientation of polarization indicates the presence of a toroidal magnetic field along the equatorial plane. Across the central cavity, no clear polarization is visible, thus any statements about the orientation of a possible magnetic field inside the bubble is impossible. If this interpretation for the rather low X-ray luminosity is correct, we must infer that heat conduction, in the particular case of NGC 7027, is not fully suppressed by the presence of a (weak) magnetic field. The field geometry is likely to play a role. Indeed, it seems that the X-ray emission is suppressed in the equatorial plane (Kastner et al. 2002).

Alternatively, the low X-ray luminosity of NGC 7027 might be related to the presence of bipolar collimated outflows found by Cox et al. (2002). It is conceivable that a significant amount of potentially X-ray emitting matter is lost through multiple openings in the skin of the hot bubble created by the jets.

NGC 2392. This is a rather peculiar object which poses a problem for our models, as already noted above. Its central star has a wind speed that is much too low for the object's position in the Hertzsprung-Russell diagram at about 40 000 K effective temperature. The wind speed is more typical for the end of the early-wind phase, although the mass-loss rate appears to be rather normal (see Table 3). This low wind speed is responsible for a wind luminosity which is about a factor of ten below the wind powers of the other objects of this study (cf. Fig. 3).

Despite of this, the X-ray emission from the hot bubble of NGC 2392 compares well with that of the other objects (cf. Fig. 16) and is much too high for an early-wind with speeds below 500 km s^{-1}, as is predicted by our models (Fig. 17). It is possible that additional X-ray emission is provided by jets as proposed by Akashi et al. (2008).

5.6. The UV emission lines

Due to the steep temperature gradient across the bubble/nebula interface, there exists only a very narrow region which is suitable for the emission of UV lines from highly ionized species. We recall here that our code computes the ionization of all elements considered (see Table 1) time-dependently for the whole computational domain, i.e. also in the freely streaming and shocked stellar wind. As a byproduct of our simulation, we are thus able to compute also the line emission from the bubble/PN interface.

Recently, Gruendl et al. (2004) reported the detection of O VI λ 1032 and 1038 Å emission lines in FUSE spectra of NGC 6543. Since the central star is not very hot, the ionization within the nebular shell is too low as to account for O^{5+}. The authors concluded that the O VI lines must originate from the conduction front at temperatures of about a few times 10^5 K.

Test calculations showed that the O^{5+} shell or "pocket" is extremely thin, only about 1×10^{15} cm thick, which is comparable with the spatial resolution of our numerical mesh. We thus recomputed the sequences Nos. 6a, 6a-HC, and 6a-HC2 with a finer mesh ($\Delta r = 3 \times 10^{14}$ cm) for $r \leq 1.5 \times 10^{17}$ cm in order to achieve a better resolution of the O^{5+} layers.

Figure 20 illustrates how the ionization of oxygen varies within the hot bubble, and how the distribution of O^{+5} depends on the physical treatment of this region. Note that, since the thermal structure of the conduction front/contact discontinuity does not change much during the lifetime of the PN, the ionization fractions remain rather stationary with respect to the front/discontinuity. We find that the thermal structure close to the conduction front where O^{5+} prevails does not differ much between our two treatments of heat conduction.

The physical conditions change rapidly across the conduction front: ahead photoionization by the stellar radiation field is the dominant heating and ionization mechanism. For the stellar temperature shown in Fig. 20, O^{2+} and O^{3+} are practically the only representatives of oxygen. Behind the front the temperatures are so high ($\gtrsim 10^5$ K) that electron collisions determine the ionization state of the gas: now we have a mixture of O^{6+}, O^{7+}, and O^{8+} in proportions ruled by the electron temperature. For instance, in the case without heat conduction the bubble temperature is so large that O^{8+} (the bare oxygen nucleus) is the main constituent already right behind the contact discontinuity. Heat conduction lowers the temperature gradient behind the front, and consequently O^{6+} and O^{7+} are the main constituents of oxygen throughout a large fraction of the bubble.

The transition between the photo-heated nebular gas ($T_e \simeq 10^4$ K) and the shock-heated wind gas ($T_e > 10^7$ K) occurs very abruptly across the contact discontinuity if there is no thermal conduction, and consequently only little room is left for the existence of O^{5+}, simply because the temperature is either too low (nebula) or too too hot (bubble). With thermal conduction included, the temperature increases somewhat more gently and thus allows for a larger amount of O^{5+}. This is also reflected in the total emission of the O VI lines listed in Table 5 for the models shown in Fig. 20. We point out that the computed O VI luminosities are strongly fluctuating from model to model due to the poor numerical resolution of the conduction front. The O VI line fluxes listed in Table 5 are therefore appropriate averages over several contiguous models.

According to the results for the heat conduction models in Table 5, the total flux in the O VI line at λ 1032 Å emitted by the O^{5+} pocket, assuming a distance of 1 kpc, would be roughly 4×10^{-13} erg cm^{-2} s^{-1}. This is consistent with the estimates of Gruendl et al. (2004) for NGC 6543, although their FUSE measurements are based on a slit across the central cavity. The total O VI λ 1032 Å line flux is certainly larger than the quoted value of $\simeq 2 \times 10^{-13}$ erg cm^{-2} s^{-1}.

We conclude that the luminosity in UV O VI lines is generated in a very thin transition layer which is not very sensitive to the effects of thermal conduction. In contrast, the X-ray luminosity depends sensitively on the efficiency of thermal conduction. In our models with heat conduction included, the O VI luminosity is comparable to the X-ray emission coming from more extended parts of the bubble (cf. Tables 3 and 5).

6. Summary and conclusions

We presented a detailed numerical approach towards an understanding of the diffuse soft X-ray emission from planetary nebulae based on the concept of thermal conduction. Since thermal conduction is a physical process inherent to all hydrodynamical systems, becoming important wherever the mean free path of the electrons is sufficiently large, we included a thermal conduction module into our 1D radiation-hydrodynamics code. We were able to compute the thermal structure of the shocked wind

Table 5. Dependence of the luminosity of the O VI lines at λ 1032 Å and 1038 Å on the treatment of heat conduction for models similar to those shown in Fig. 4, but computed with higher spatial resolution. L(Hβ) and L(O III 5007 Å) refer to the Hβ and [O III] luminosities of the whole nebula.

No.	M ($M_\odot$)	L ($L_\odot$)	$T_{\rm eff}$ (K)	Thermal conduction	L(Hβ) ($L_\odot$)	L(O III 5007 Å) ($L_\odot$)	L(O VI 1032 Å) ($L_\odot$)	L(O VI 1038 Å) ($L_\odot$)
6a-HR	0.595	5260	67 978	no	21.7	168.8	4.41×10^{-3}	2.21×10^{-3}
6a-HCHR	0.595	5297	65 160	method 1	23.9	174.0	11.3×10^{-3}	5.63×10^{-3}
6a-HC2HR	0.595	5292	65 541	method 2	23.6	173.3	10.1×10^{-3}	5.04×10^{-3}

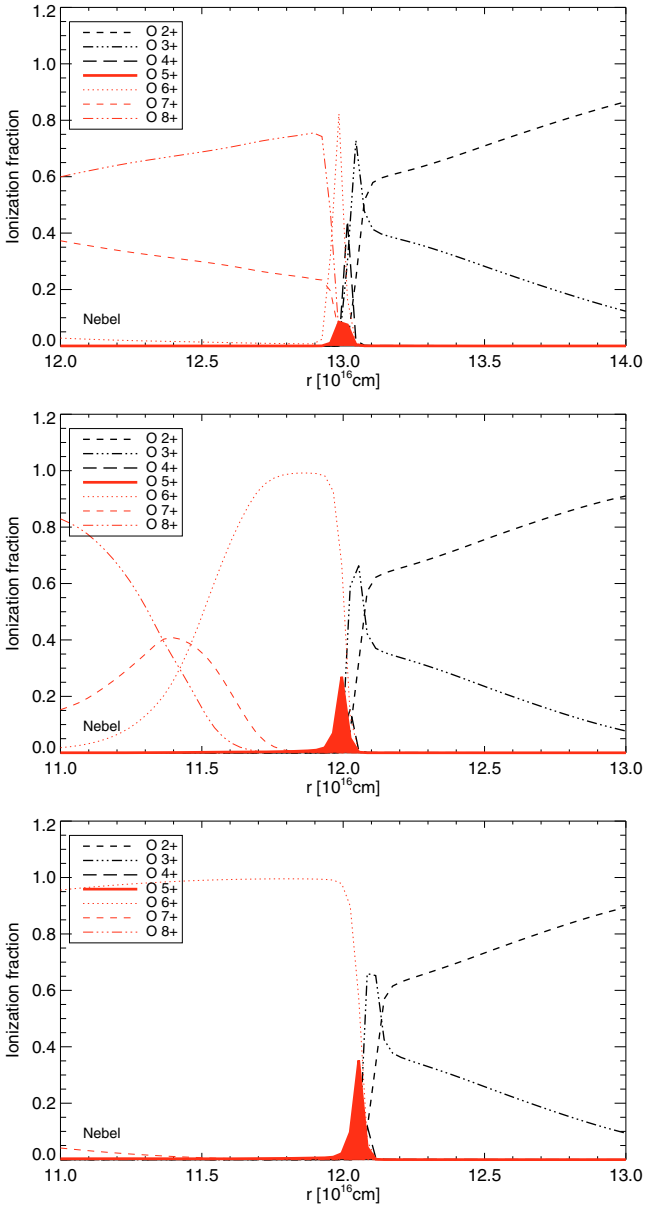

Fig. 20. Radial profiles of the ionization fractions of oxygen in the vicinity of the contact discontinuity/conduction front for different physical treatments: *Top*: without thermal conduction; *middle*: with thermal conduction according to method 1; *bottom*: with thermal conduction according to method 2. Thick lines refer to the nebular region, thin ones to the bubble region behind the contact surface/conduction front. The very thin O^{5+} "pocket" is shaded for clarity. Details about the three models are given in Table 5.

gas inside the nebular cavity self-consistently with the hydrodynamics once the stellar AGB remnant, its initial circumstellar envelope, and the post-AGB wind model are specified. By doing so, there is some freedom in the treatment of heat conduction in cases where the mean free path of the electrons becomes comparable to the characteristic temperature scale length. Magnetic fields that may play a role for the shaping of PNe are not considered.

Thermal conduction has a twofold effect favoring thermal X-ray emission from the shocked wind gas: it lowers the temperature gradient across the bubble/nebula interface and heats the cool nebular matter, forcing it to "evaporate" inwards. With time, heat conduction accumulates additional matter in the bubble with a characteristic temperature of some 10^6 K, which quickly dominates the bubble's mass budget. The amount of added matter is controlled by heat transfer across the bubble from the inverse wind shock towards the nebula. The bubble mass may increase or decrease with time, depending on the evolution of the stellar wind power.

We selected several of the hydrodynamic sequences presented in Paper I and recomputed them, without changing any of the other parameters or boundary conditions, with our heat conduction treatment included. The X-ray emission was computed post-facto by employing the CHIANTI code, slightly adapted to match our purposes. We were able to find good agreement with existing observations, both with respect to X-ray luminosity and surface brightness distribution, if method 2 is used for the treatment of heat conduction. At the same time, the stellar wind model employed here, based on the theory of radiation-driven winds, implies wind speeds in excess of 1000 km s^{-1} for typical nebular models (cf. Fig. 17). We conclude that our modeling is fully consistent with both the observed wind speeds of more than 1000 km s^{-1} *and* the observational evidence that the soft X-ray emission comes from regions with electron temperatures of about 2×10^6 K (see also Table 3). In contrast, our models without heat conduction fail to reproduce the characteristics of the observed X-ray emission by large amounts if realistic wind parameters are assumed.

The basic findings from our modeling can be summarized as follows:

- The energy budget of the hot bubble is substantially altered by radiative losses at the bubble/nebula interface, both in models with and without thermal conduction.
- Heat conduction has a strong influence on the thermal structure of the hot bubble, but leaves the dynamics of the whole system is virtually unchanged, i.e. the shaping of the nebular shells and their expansion properties are not affected.
- In the absence of heat conduction, the temperature of the hot bubble depends only on the velocity of the central star wind. The resulting X-ray temperature is much too high, and the X-ray luminosity much too low, to explain the existing observations.
- If heat conduction is substantial, the bubble temperature is a function of the stellar wind power and the bubble size. The compact nebulae around massive, short-lived central stars

are therefore expected to have hotter bubbles than the nebulae of low-mass, slowly evolving central stars.
- The X-ray luminosity is determined by the total emission measure, which decreases by expansion and increases by "evaporation" from the main nebula. The competition between expansion *and* "evaporation" rules the temporal evolution of the X-ray luminosity.
- According to our PN simulations with a time-dependent wind model, the X-ray luminosities increase with time during the main phase of evolution when the wind power increases with time, in contrast to the case of a constant wind power that would imply a decrease of the X-ray luminosity with time.
- For the energy range usually considered for planetary nebulae, the X-ray luminosity is below about 1% of the stellar wind power, and between 10^{-4} and 10^{-8} of the stellar bolometric luminosity. The exact numbers depend on the actual evolutionary state and the wind model used.
- For given effective temperature, the X-ray emission is largest for nebulae around massive central stars even though their small bubbles contain only little mass. The X-ray emission measure of their bubbles is nevertheless large, primarily because the high electron densities overcompensate the small amount of X-ray emitting gas that massive central stars can accumulate during their short lifetimes.
- In contrast to the X-ray luminosity, the emission of the UV O VI lines is not very sensitive to the effects of thermal conduction.
- Magnetic fields must be absent or extremely weak in all objects with diffuse X-ray emission since their presence would strongly depress thermal conduction and hence "evaporation". The absence or weakness of magnetic fields implies also that they cannot be responsible for shaping these objects.

Our numerical treatment as described here leads to X-ray luminosities that are substantially below those found by Zhekov & Perinotto (1998, 1996) with their analytical approach, although their wind model and central-star evolution are very similar. We believe that their analytical approach overestimates the evaporation rate because radiative cooling of the gas at the conduction front by line emission is not considered (see also Sect. 3.3).

It is likely that the bubble/PN interface becomes dynamically unstable, leading to direct mixing between hot bubble and cool nebular matter (cf. Stute & Sahai 2006). The net effect would be similar to heat conduction, i.e. a reduction of temperature gradients allowing a more efficient X-rays emission, as already mentioned by Chu et al. (1997). The 2D simulations of a spherical bubble performed by Stute & Sahai (2006) suggest that the mixing region is confined to a rather thin shell at the surface of the bubble. If so, the X-ray emission would be limb brightened, very similar to our models computed according to method 1. For the time being, the existing observations do not seem to be consistent with such a limb brightening.

Georgiev et al. (2008) found recently that the wind of the central star of NGC 6543 is less depleted in iron compared to the plasma emitting the diffuse X-rays (Georgiev et al. 2006). They concluded that the X-ray emitting plasma "is derived from nebular gas rather than the stellar wind". This finding is fully consisting with the heat-conduction models. Clearly, more studies of this kind would be very rewarding.

Finally we want to emphasise that the models introduced in this work are entirely based on normal chemical compositions in the stellar and circumstellar envelopes. The results presented here should therefore *not* be used to interprete X-ray emission from objects with hydrogen-deficient central stars such as BD+30°3639, NGC 40 because their evolution is different and not yet understood. Additionally, one has to deal with heat conduction and X-ray emission in a practically hydrogen-free plasma.

Acknowledgements. We are grateful to Dr. A. Schwope for introducing us to the secrets of the EPIC camera on board XMM-Newton and providing us with the response matrix. We are especially thankful to Dr. Landi who helped us to install the latest version of the CHIANTI code. The work of A.W. was supported by DLR under grant No. 50 QL 0001.

References

Akashi, M., Soker, N., & Behar, E. 2006, MNRAS, 368, 1706
Akashi, M., Soker, N., Behar, E., & Blondin, J. 2007, MNRAS, 375, 137
Akashi, M., Meiron, Y., & Soker, N. 2008, [arXiv:0711.3265]
Borkowski, K. J., Balbus, S. A., & Fristrom, C. C. 1990, ApJ, 355, 501
Castor, J., McCray, R., & Weaver, R. 1975, ApJ, 200, L107
Chu, Y.-H., Chang, T. H., & Conway, G. M. 1997, ApJ, 482, 891
Chu, Y.-H., Guerrero, M. A., & Gruendl, R. 2003, in Planetary Nebulae: Their Evolution and Role in the Universe, ed. S. Kwok, M. Dopita, & R. Sutherland, IAU Symp., 209, 415
Corradi, R. L. M., Schönberner, D., Steffen, M., & Perinotto, M. 2003, MNRAS, 340, 417
Cowie, L. L., & McKee, C. F. 1977, ApJ, 211, 135
Cox, P., Huggins, P. J., Maillard, J.-P., et al. 2002, A&A, 384, 603
Dere, K. P., Landi, E., Mason, H. E., Monsignori Fossi, B. C. & Young, P. R. 1997, A&AS, 125, 149
Georgiev, L. N., Richer, M. G., Arrieta, A., & Zhekov, S. A. 2006, ApJ, 639, 185
Georgiev, L. N., Peimbert, M., Hillier, D. J., Richer, M. G., Arrieta, A., & Peimbert, A. 2008 [arXiv:0802.3692]
Gruendl, R. A., Chu, Y.-H., & Guerrero, M. A. 2004, ApJ, L127
Guerrero, M. A. 2006, in Planetary Nebulae in our Galaxy and Beyond, ed. M. J. Barlow, & R. H. Méndez, IAU Symp., 234, 153
Guerrero, M. A., Chu, Y.-H., & Gruendl, R. 2005a, in Planetary Nebulae as Astronomical Tools, ed. R. Szczerba, G. Stasińska, & S. Górny, AIP Conf. Proc., 804, 157
Guerrero, M. A., Chu, Y.-H., Gruendl, R., & Meixner, M. 2005b, A&A, 430, L69
Kastner, J. H. 2007, in Asymmetrical Planetary Nebulae IV, ed. R. L. M. Corradi et al., [arXiv:0709.4136]
Kastner, J. H., Vrtilek, S. D., & Soker, N. 2001, ApJ, 550, L189
Kastner, J. H., Jingquiang, L., Vrtilek, S. D., et al. 2002, ApJ, 581, 1225
Kastner, J. H., Montez, Jr., R., Balick, B., & De Marco, U. 2008, ApJ, 672, 957
Koo, B.-C., & McKee, C. F. 1992, ApJ, 388, 103
Kudritzki, R.-P., Urbaneja, M. A., & Puls, J. 2006, in Planetary Nebulae in our Galaxy and Beyond, ed. M. J. Barlow, & R. H. Méndez, IAU Symp., 234, 119
Landi, E., & Phillips, K. J. H. 2005, ApJS, 160, 286
Marten, H., & Szczerba, R. 1997, A&A, 248, 590
Mazzotta, P., Mazzitelli, G., Colafrancesco, S., & Vittorio, N. 1998, A&AS, 133, 403
Mellema, G., & Frank, A. 1995, MNRAS, 273, 401
Méndez, R. H., Kudritzki, R. P., & Herrero, A. 1992, A&A, 260, 329
Morrison, R., & McCammon, D. 1983, ApJ, 270, 119
Pauldrach, A. W. A., Puls, J., Kudritzki, R. P., Méndez, R. M., & Heap, S. H. 1988, A&A, 207, 123
Pauldrach, A. W. A., Hoffmann, T. L., & Méndez, R. M. 2004, A&A, 419, 1111
Perinotto, M., Kifonidis, K., Schönberner, D., & Marten, H. 1998, A&A, 332, 1044
Perinotto, M., Schönberner, D., Steffen, M., & Calonaci, C. 2004, A&A, 414, 993 (Paper I)
Reed, D. S., Balick, B., Haijan, A. R., et al. 1999, AJ, 118, 2430
Reimers, D. 1975, in Problems in Stellar Atmospheres and Envelopes, ed. B. Baschek, W. H. Kegel, & G. Traving (Berlin: Springer), 229
Ruiz, N., Guerrero, M. A., Chu, Y.-H., et al. 2006, in Planetary Nebulae in our Galaxy and Beyond, ed. M. J. Barlow, & R. H. Méndez, IAU Symp., 234, 497
Sabin, L., Zijlstra, A. A., & Greaves, J. S. 2007, MNRAS, 376, 378
Sandin, C., Schönberner, D., Roth, M. M., et al. 2008, A&A, in press
Schönberner, D., & Steffen, M. 2003, in Planetary Nebulae: Their Evolution and Role in the Universe, ed. S. Kwok, M. Dopita, & R. Sutherland, IAU Symp., 209, 147

Schönberner, D., Steffen, M., Stahlberg, J., Kifonidis, K., & Blöcker, T. 1997, in Advances of Stellar Evolution, ed. R. T. Rood, & A. Renzini (Cambridge Univ. Press), 146
Schönberner, D., Jacob, R., & Steffen, M. 2005a, A&A, 441, 573
Schönberner, D., Jacob, R., Steffen, M., Perinotto, M., Corradi, R. L. M., & Acker, A. 2005b, A&A, 431, 963
Schönberner, D., Steffen, M., & Warmuth, A. 2006, in Planetary Nebulae in our Galaxy and Beyond, ed. M. J. Barlow, & R. H. Méndez, IAU Symp., 234, 161
Soker, N. 1994, AJ, 107, 276
Soker, N., & Kastner, J. H. 2003, ApJ, 583, 368
Spitzer, L. 1962, Physics of Fully Ionized Gases, 2nd revised edition (Wiley Interscience Publishers)
Steffen, M., & Schönberner, D. 2006, in Planetary Nebulae in our Galaxy and Beyond, ed. M. J. Barlow & R. H. Méndez, IAU Symp., 234, 285
Steffen, M., Szczerba, R., & Schönberner, D. 1998, A&A, 337, 149
Stute, M., & Sahai, R. 2006, ApJ, 651,882
Tinkler, C. M., & Lamers, H. J. G. M. 2002, A&A, 384, 987
Tsamis, Y. G., Walsh, J. R., Péquignot, D., et al. 2008, MNRAS, 386, 22
Volk, K., & Kwok, S. 1985, A&A, 153, 79
Weaver, R., McCray, R., Castor, J., Shapiro, P., & Moore, R. 1977, ApJ, 218, 377
Wrigge, M., Wendker, H. J., & Wisotzki, L. 1994, A&A, 286, 219
Zhekov, S. A., & Perinotto, M. 1996, A&A, 309, 648
Zhekov, S. A., & Perinotto, M. 1998, A&A, 334, 239